Theses and Dissertations | 1. Thesis and Dissertation Collection, all items

1990-06

Analysis of the ultraviolet emissions of nitric oxide from mid-latitude rocket observations

Clayton, Michael J.

Monterey, California: Naval Postgraduate School

http://hdl.handle.net/10945/27728

NAVAL POSTGRADUATE SCHOOL

Monterey, California

THESIS

ANALYSIS OF THE ULTRAVIOLET EMISSIONS
OF NITRIC OXIDE FROM
MID-LATITUDE ROCKET OBSERVATIONS

by

Michael J. Clayton

June, 1990

Thesis Advisor: David D. Cleary

Approved for public release; distribution is unlimited.

91-03065

REPORT DOCUMENTATION PAGE

1a REPORT SECURITY CLASSIFICATION	1b RESTRICTIVE MARKINGS
Unclassified	

2a. SECURITY CLASSIFICATION AUTHORITY	3 DISTRIBUTION / AVAILABILITY OF REPORT
2b DECLASSIFICATION / DOWNGRADING SCHEDULE	Approved for public release; distribution is unlimited

4 PERFORMING ORGANIZATION REPORT NUMBER(S)	5 MONITORING ORGANIZATION REPORT NUMBER(S)

6a. NAME OF PERFORMING ORGANIZATION	6b OFFICE SYMBOL (If applicable)	7a NAME OF MONITORING ORGANIZATION
Naval Postgraduate School	33	Naval Postgraduate School

6c. ADDRESS (City, State, and ZIP Code)	7b. ADDRESS (City, State, and ZIP Code)
Monterey, CA 93943-5000	Monterey, CA 93943-5000

8a. NAME OF FUNDING / SPONSORING ORGANIZATION	8b OFFICE SYMBOL (If applicable)	9. PROCUREMENT INSTRUMENT IDENTIFICATION NUMBER

8c. ADDRESS (City, State, and ZIP Code)	10 SOURCE OF FUNDING NUMBERS			
	PROGRAM ELEMENT NO.	PROJECT NO.	TASK NO	WORK UNIT ACCESSION NO

11. TITLE (Include Security Classification) ANALYSIS OF THE ULTRAVIOLET EMISSIONS OF NITRIC OXIDE FROM MID-LATITUDE ROCKET OBSERVATIONS

12 PERSONAL AUTHOR(S) Clayton, Michael J.

13a. TYPE OF REPORT	13b TIME COVERED	14 DATE OF REPORT (Year, Month, Day)	15 PAGE COUNT
Master's Thesis	FROM ___ TO ___	June, 1990	68

16. SUPPLEMENTARY NOTATION The views expressed in this thesis are those of the author and do not reflect the official policy or position of the Department of Defense or the U.S. Government.

17	COSATI CODES		18 SUBJECT TERMS (Continue on reverse if necessary and identify by block number)
FIELD	GROUP	SUB-GROUP	Ultraviolet Spectra; Dayglow; Nitric Oxide

19 ABSTRACT (Continue on reverse if necessary and identify by block number)

Ultraviolet emissions of the Earth's ionosphere in the wavelength range of 2000 A to 2500 A are analyzed. These data were obtained by a rocket-borne spectrograph flown on March 30, 1990 from the White Sands Missile Range, New Mexico. The gamma and epsilon bands of nitric oxide dominate this portion of the spectrum. Column densities of nitric oxide are determined by fitting eleven of the most prominent bands with synthetic spectra. Additionally, a temperature profile is found between the altitudes of 145 km and 195 km. From the data, corrections to the Franck-Condon factors are determined for three v" progressions of the nitric oxide gamma bands.

20 DISTRIBUTION / AVAILABILITY OF ABSTRACT	21 ABSTRACT SECURITY CLASSIFICATION
☐ UNCLASSIFIED/UNLIMITED ☒ SAME AS RPT ☐ DTIC USERS	Unclassified

22a NAME OF RESPONSIBLE INDIVIDUAL	22b TELEPHONE (Include Area Code)	22c OFFICE SYMBOL
David D. Cleary	(408) 646-2828	61-Cl

i

Analysis of the Ultraviolet Emissions
of Nitric Oxide from
Mid-Latitude Rocket Observations

by

Michael J. Clayton
Lieutenant, United States Navy
B.A., University of California at Berkeley

Submitted in partial fulfillment
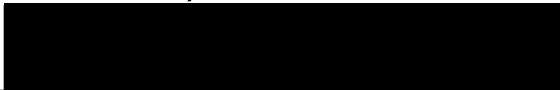of the requirements for the degree of
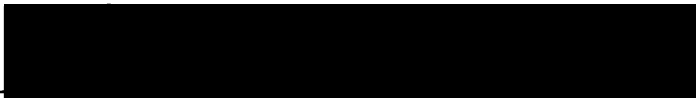
MASTER OF SCIENCE IN PHYSICS

from the

NAVAL POSTGRADUATE SCHOOL
June 1990

Author: _____
Michael J. Clayton

Approved by: _____
David D. Cleary, Thesis Advisor

_____
Suntharalingam Gnanalingam, Second Reader

_____
Karlheinz E. Woehler, Chairman, Department of Physics

ii

ABSTRACT

Ultraviolet emissions of the Earth's ionosphere in the wavelength range of 2000 Å to 2500 Å are analyzed. These data were obtained by a rocket-borne spectrograph flown on March 30, 1990 from the White Sands Missile Range, New Mexico. The gamma and epsilon bands of nitric oxide dominate this portion of the spectrum. Column densities of nitric oxide are determined by fitting eleven of the most prominent bands with synthetic spectra. Additionally, a temperature profile is found between the altitudes of 145 km and 195 km. From the data, corrections to the Franck-Condon factors are determined for three v'' progressions of the nitric oxide gamma bands.

iii

TABLE OF CONTENTS

LIST OF FIGURES

I. INTRODUCTION

The electromagnetic properties of the Earth's ionosphere are important to many military applications, such as HF radio communications and over-the-horizon radar. These properties depend on the ionosphere's electron density profile, which varies over time, altitude, and geographic location. Currently, ground based ionosondes are used to measure the ionospheric electron density. This technique is accurate and fast, but spatially limited. Global electron density maps are based on the profiles from only a few sites. True global measurements are desired. As satellite-based ionosondes are impractical, efforts are being directed towards other potential worldwide sensing methods.

Observation of the Earth's airglow spectra is such a technique. The principal ions in the lower thermosphere are chemically coupled to the various neutral molecules and atoms present. The densities of the neutral species can be determined from measurements of the ultraviolet emission spectrum of the ionosphere. Electron densities can then be inferred from these measurements.

This thesis presents an analysis of the ultraviolet emissions of nitric oxide (NO) in the Earth's atmosphere. These emissions were observed by the Naval Postgraduate School's Middle Ultraviolet Spectrograph (MUSTANG) experiment flown aboard a NASA sounding rocket. The experiment is part of an ongoing effort to develop passive remote sensing techniques.

A. THESIS OBJECTIVES

This work focuses on thirteen averaged spectra obtained by the MUSTANG experiment over an altitude range of 100 to 200 kilometers. Nitric oxide emissions with wavelengths from 2000 Å to 2500 Å are examined. Each observed spectrum is modeled by a synthetic spectrum in which the relative strengths of the most prominent gamma and epsilon band transitions are varied independently. Eleven emission features of NO are identified and analyzed in the wavelength range of interest.

The goal of the analysis is to determine the column density of nitric oxide at each altitude. A first step in this process is to obtain a temperature profile from the data. These temperatures are used for the rest of the fitting procedure.

B. THESIS OUTLINE

The thesis is divided into six chapters. Chapter II gives some background on the stratification of the atmosphere as well as some fundamentals of nitric oxide chemistry in the lower ionosphere. In Chapter III, a brief review of diatomic molecular spectra is presented. Application of the results to the calculation of the synthetic spectra is discussed.

Chapter IV describes the experiment and the MUSTANG instrument used in obtaining the spectra. The data are also presented. These data are analyzed in Chapter V. Each observed spectrum is fitted with a synthetic spectrum as closely as possible. Causes for variations between the model and the observed spectra are discussed. Chapter VI concludes with a summary of the findings and suggestions for further research.

II. BACKGROUND

A. INTRODUCTION

Although nitric oxide is a trace element in the atmosphere, it plays a major role in atmospheric chemistry. In the stratosphere and mesosphere, it has been noted that NO acts as a catalyst in the destruction of ozone (O_3). The low first ionization potential of nitric oxide makes it an important source of ions in the lower ionosphere. The ionization of nitric oxide by the solar Lyman-α emission at 1216 $\overset{\circ}{A}$ is responsible for the formation of the D region of the ionosphere. A brief description of the earth's atmosphere, ionosphere and nitric oxide chemistry follows.

B. THE NEUTRAL ATMOSPHERE

Variations in the Earth's atmosphere are caused by differential heating from solar radiation, convective mixing, and the rotation of the Earth. There results a limited stratification of the atmosphere which is commonly described in two ways; either in terms of the temperature gradients in the atmosphere or by the chemical composition.

As shown in Figure 2-1, temperature gradients divide the atmosphere into four basic regions. The troposhere occupies the lowest ten kilometers of the atmosphere and is characterized by a steady decrease in temperature with height. It is in this region that our "weather" occurs. After passing through an isothermal region, the temperature begins to increase with altitude up to 45 kilometers. This region is known as the stratosphere.

3

Above this, in the mesosphere, the temperature again decreases to about 180 K at an altitude of 5 kilometers. This is the coldest region of the atmosphere. Above the mesosphere, the kinetic temperature of the atmosphere increases with altitude towards a value dependent on solar activity. This region is known as the thermosphere
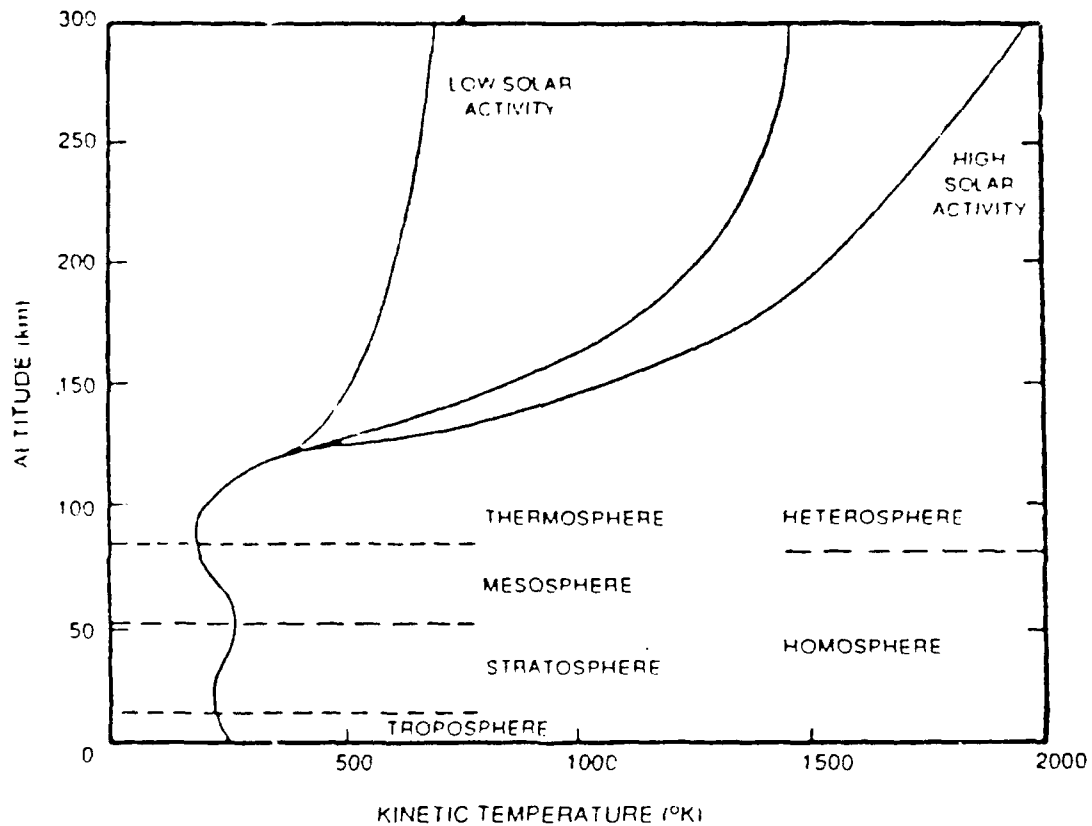
Figure 2-1 Temperature and Composition of the Atmosphere (Tascione, 1988)

The lower boundary of the thermosphere marks a division between two chemical composition regions of the atmosphere. The troposhere, stratosphere, and mesosphere all make up the region known as the homosphere. The homosphere is composed of approximately 78% nitrogen, 21% oxygen, and 1% of other gases. Mixing in the homosphere keeps the relative densities of these gases nearly constant throughout the

4

region. Above 100 kilometers, the combination of low densities and the stable temperature gradient cause mixing to cease. Each atmospheric contituent reaches its own separate hydrostatic equilibrium. The relative densities of the gases change with altitude, giving this region the name heterosphere. From 500 kilometers to an indefinite limit lies the exosphere, a region of high kinetic energies and low densities.

C. THE IONOSPHERE

Above 50 kilometers, photoionization and low recombination rates produce a partially ionized region known as the ionosphere. This region is divided on the basis of free electron densities into the D, E, F_1, and F_2 layers. These layers form due to changes in the composition and solar absorption characteristics of the atmosphere. Electron concentrations in the ionosphere vary with solar activity. The ultraviolet and x-ray output of the Sun has been correlated with the solar flux at 2800 MHz. Commonly called F10.7, this value is measured daily and is taken as a standard indicator of solar activity.

The D region of the ionosphere extends from about 50 to 90 km in altitude. As the lowest lying region of the ionosphere, it is produced by the deepest penetrating ionizing radiation incident on the atmosphere. The major source of ions is from the ionization of NO by the Lyman-α emission at 1216 Å.

The E region is generally taken to lie between 90 and 130 km. The electron density is due primarily to the photoionization of molecular oxygen by Lyman-β and and soft solar x-rays. It has a daytime electron density two orders of magnitude higher than the D region's.

In the F regions, the principal ion is O^+, formed by the photoionization of atomic oxygen. Molecular oxygen and nitrogen also contribute. The F_1 region is characterized by a relatively constant electron density. In the F_2 region, which lies above 160 km, the electron density reaches its maximum value.

The presence of nitric oxide in the lower ionosphere is a result of the interaction of solar radiation with the atmosphere. Processes which lead to the dissociation of N_2 are the source of what is known as the odd nitrogen family. This family consists of all photochemically active nitrogen containing species. Of these, nitric oxide is the most abundant.

The mechanisms leading to the production and loss of odd nitrogen will not be explored in this thesis, but the chemical reactions have been tabulated by Cleary (1986). Figure 2-2 is a schematic representation of these reactions in the thermosphere. The figure shows that the production of odd nitrogen is a photolytically driven process. Photons and photoelectrons interact with the major constituents of the atmosphere, forming O_2^+, O^+, and N_2^+. In turn, chemical interaction of these ions with the atmosphere and the solar flux produce the odd nitrogen family. Many of these reactions terminate at NO^+, whose only significant loss mechanism is dissociatve recombination. Figure 2-2 also shows that while $N(^2D)$ is a source for neutral NO, $N(^4S)$ is both a source and a sink. The abundance of nitric oxide is sensitive to the production rate of $N(^2D)$.

6

IONOSPHERIC ODD-NITROGEN PHOTOCHEMISTRY
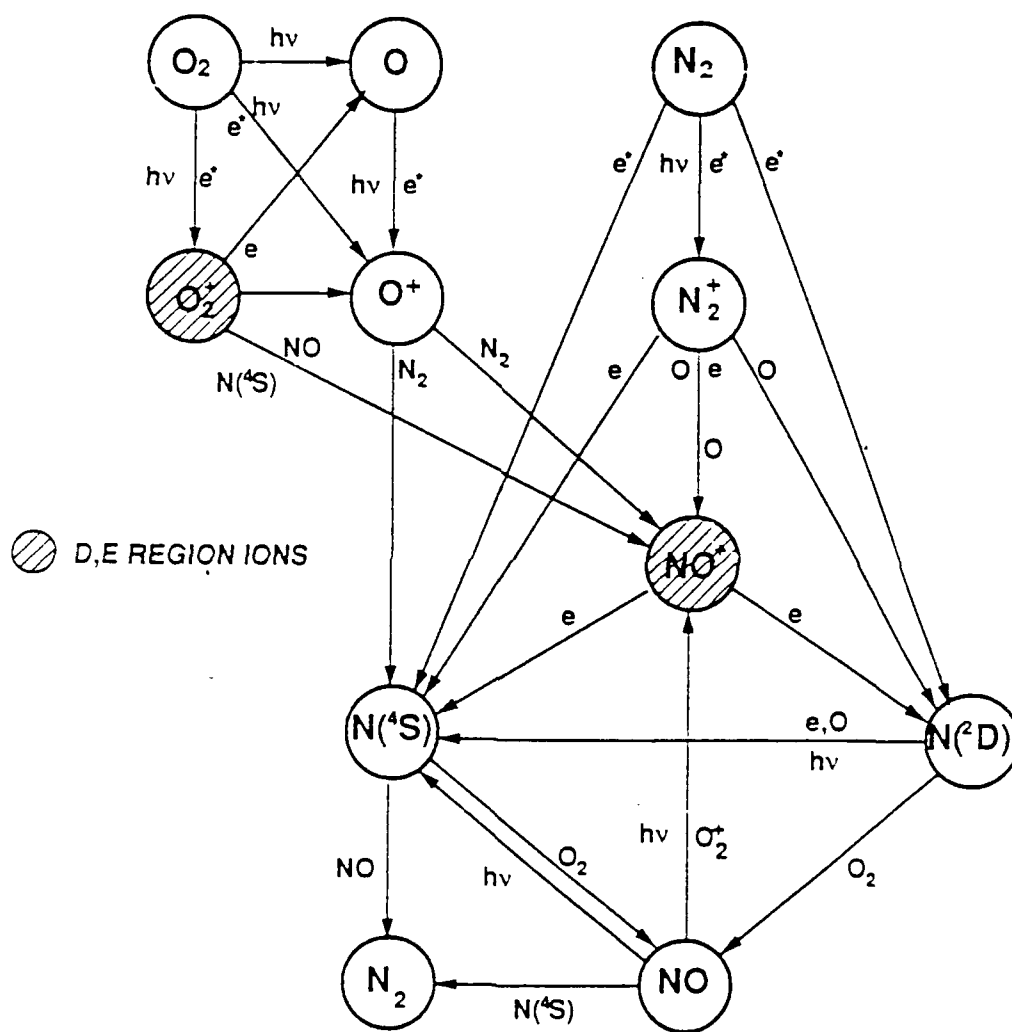
Figure 2-2 Ionospheric Odd Nitrogen Photochemistry

III. DIATOMIC MOLECULAR SPECTRA

A. INTRODUCTION

Spectroscopic analysis is a useful tool which has been applied to a variety of fields. From the spectral emission and absorption features of a gas, one can determine its chemical composition and physical conditions. Study of the Earth's atmospheric dayglow provides a means to map the ionosphere in terms of composition, temperature, and reaction processes for various altitudes and geographic latitudes.

To better understand the data and the development of the synthetic spectra, a brief review of diatomic molecular spectra is presented. A very thorough treatment of this subject is given by Herzberg (1950).

B. DIATOMIC MOLECULES

The simplest model of the diatomic molecule is a dumbbell in which two spheres of mass M_1 and M_2 are separated by a distance and bound by electrostatic attraction. In addition to the electronic motion, the molecule has two possible modes; vibrational and rotational motion. From quantum mechanics, it is known that these motions cannot take on arbitrary values, but rather are quantized. The energies of the motion can be expressed as term values, where the term value is the energy divided by hc. The rotational term value, F(J), is given approximately by F(J) = BJ(J+1), where J is the rotational quantum number (J=0,1,2,...) and B is a constant of the molecule. Likewise, the vibrational term

value is given approximately by $G(v) = \omega(v+\tfrac{1}{2})$, where v is the vibrational quantum number. These approximations do not account for the anharmonic or non-rigid nature of the actual motion. However, for a given electronic state with vibrational level v and rotational level J, the term value for the combined motion can still be written as

$$T = T_e + G(v) + F(J) \tag{3-1},$$

where T_e is the electronic energy. The electronic, vibrational, and rotational states of a molecule combine in a nested manner. Figure 3-1 represents the relationship between the energy levels.

The orbital configuration of the molecule's electrons determine its electronic energy. As in atoms, the electrons form a total resultant orbital angular momentum L and a resultant spin angular momentum S. Since the electrostatic field of the molecule is symmetric along the internuclear axis, L will precess about the axis of symmetry. However, the value of L along the internuclear axis is a constant of the motion and is denoted by M_L (= L, $L-1$,...,$-L$). The magnitude of M_L is given the symbol Λ.

The resultant spin S is not affected by the molecular electrostatic field. It precesses about the internuclear axis only if there is a magnetic field present. For $\Lambda \neq 0$, there is an internal magnetic field, and S precesses about the axis of symmetry with a constant component, M_s. Designated Σ, it can take the values S, $S-1$,..., $-S$, giving a multiplicity of $(2S+1)$.

The spectroscopic notation for molecules is completely analogous to that of atoms. The total orbital angular momentum is given a Greek letter Σ, Π, Δ,... corresponding to

9

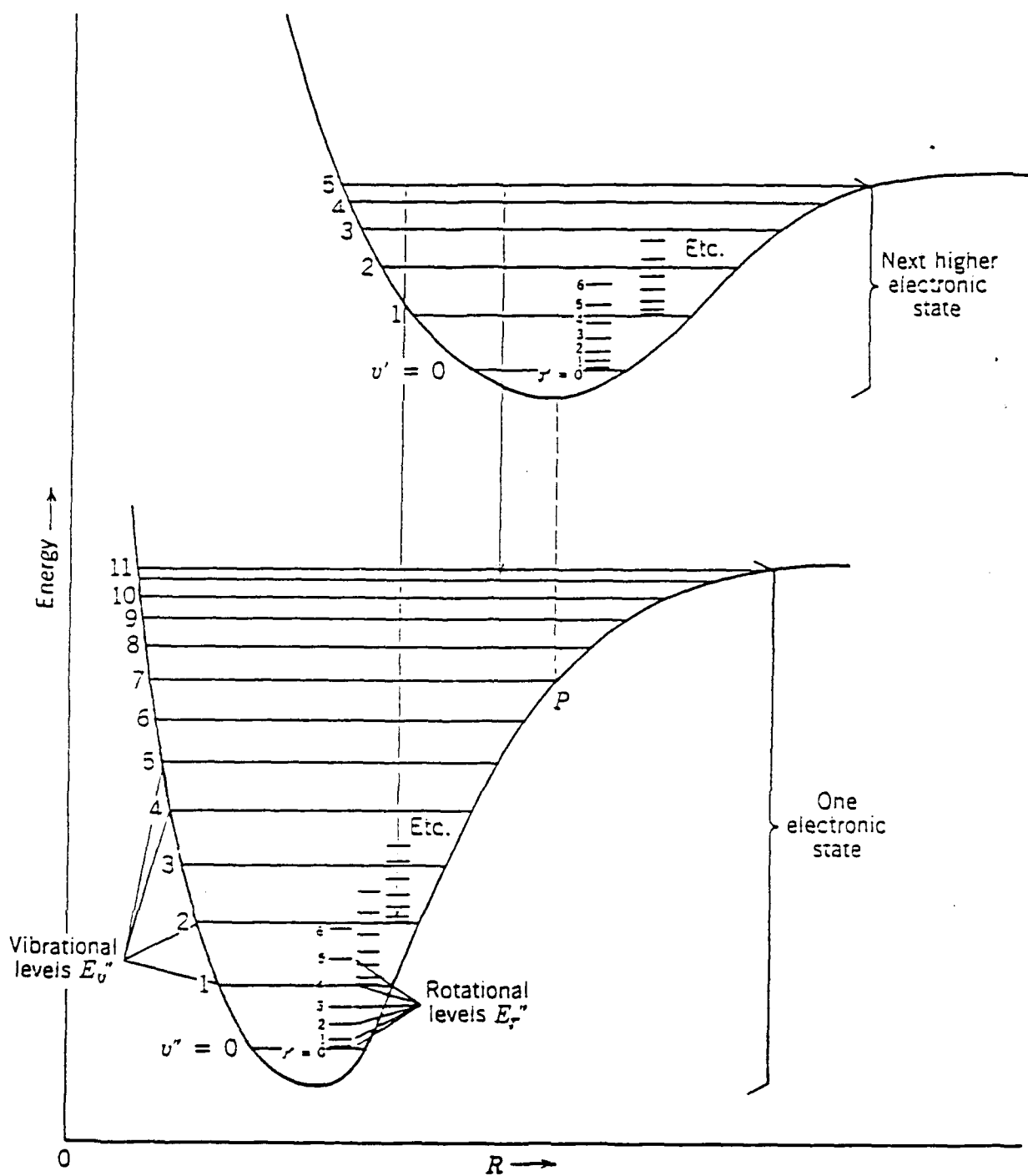**Figure 3-1** Electronic, Vibrational, and Rotational Energy Levels (Eisberg and Resnick, 1985)

10

L = 0, 1, 2,.. respectively. The multiplicity of the state is written as a left superscript. When Σ is defined ($\Lambda \neq 0$), the value ($\Lambda + \Sigma$) is written as a right subscript. Furthermore, the electronic states are labelled by letters. The ground state is traditionally given the letter X, and excited states of the same multiplicity are designated by A, B, C, etc. States with different multiplicity are labeled by lower case letters.

Figure 3-2 is a potential energy diagram for nitric oxide labelled with the spectroscopic notation. The transitions of interest to this analysis are the gamma and epsilon bands. The gamma band refers to the transition between the $A^2\Sigma$ and $X^2\Pi$ states. Similarly, the epsilon band refers to the $D^2\Sigma$ to $X^2\Pi$ transition.

C. LINE POSITIONS

The line position, σ, or wave number of a spectral emission line is given by the difference in term values between the initial and final states. The line position of a transition from the (T_e', v', J') state to the (T_e'', v'', J'') state is given by

$$\sigma = T'_e - T''_e + G'(v') - G''(v'') + F'(J') - F''(J'') \tag{3-2}$$

where the single prime refers to the upper state and the double prime refers to the lower state.

The set of transitions for which T_e' and T_e'' are fixed are called a molecular band system. Within a given band system, the transitions for which v' is fixed and v'' varies are known as a v'' band progression.
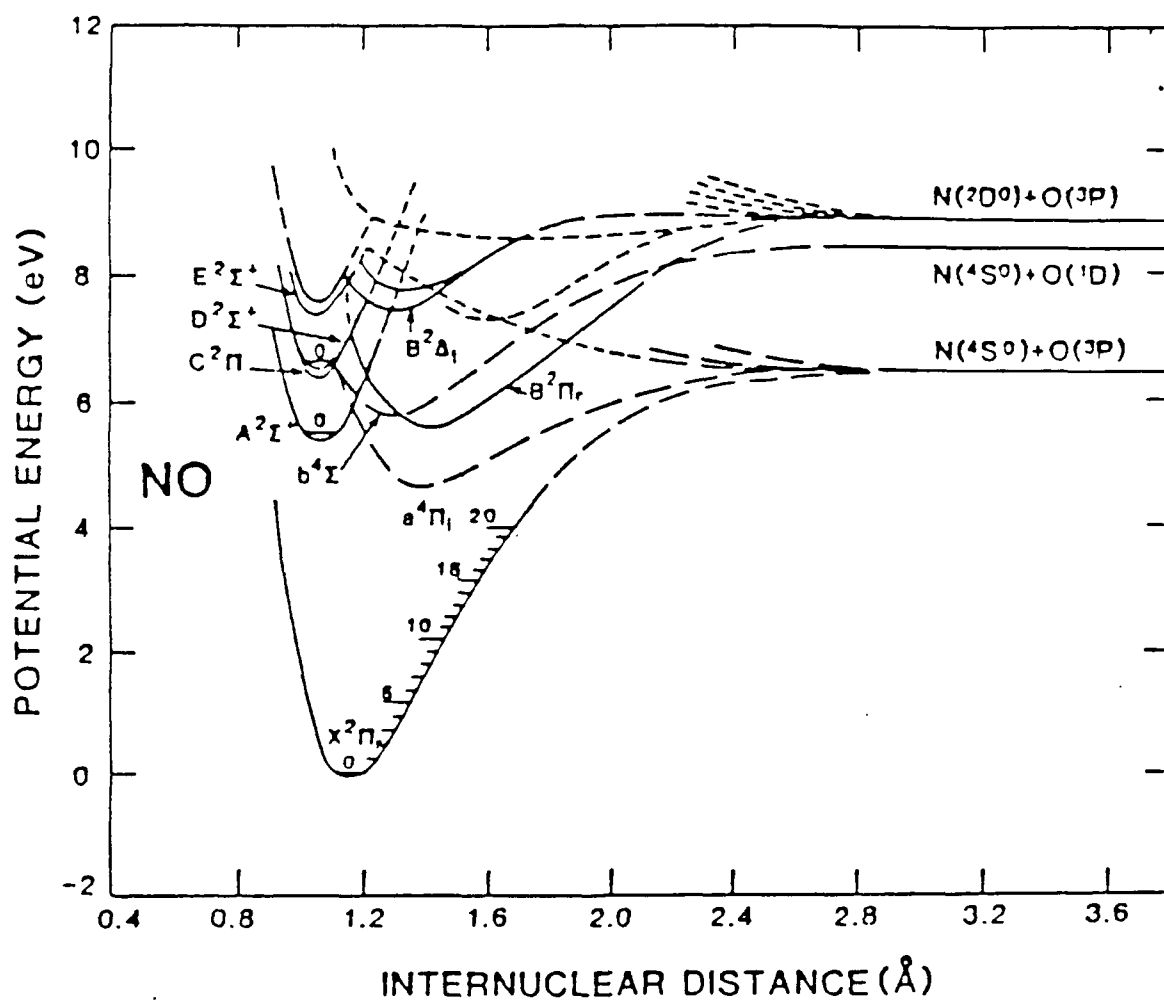
11

Figure 3-2 Potential Energy Diagram of NO (from Gilmore, 1965)

To arrive at the correct expressions for G(v) and F(J), one must account for the anharmonicity of the oscillations and the mutual influence of the rotational and electronic angular momenta. The electronic and rotational angular momenta of the molecule can couple in many ways. The form of F(J) depends on the type of coupling. That development will not be presented here.

D. EMISSION RATES

The volume emission rate for a single molecular line can be written as

$$E(n'v'J', n''v''J'') = N(n'v'J') A(n'v'J', n''v''J'') \qquad (3\text{-}3),$$

where E is the volume emission rate, N is the fractional population of the state defined by the quantum numbers n', v', J', and A is the Einstein coefficient for spontaneous emission between the given states.

The number of molecules in the level defined by n' and v' is called N(n'v'). In the steady state, this number is given by

$$N(n'v') = \frac{P(n'v')}{\sum_{v''} A_{v'v''}} \qquad (3\text{-}4),$$

where P(n'v') is the excitation rate to the (n'v') state, and the denominator is the sum over all the loss processes. Using this, equation (3-3) can be rewritten as

13

$$E(n'v'J',n''v''J'') = P(n'v') \frac{N(n'v'J')}{N(n'v')} \frac{A_{J'J''}}{\sum_{v''} A_{v'v''}} \qquad (3\text{-}5).$$

The principal excitation mechanism for NO is fluorescent scattering. The production rate is proportional to the solar flux and the effective cross section for transitions. The branching ratio into the vibrational levels is given by the Franck-Condon factors. Assuming that the absorbing molecules are all in the ground state, this gives

$$P(n'v') = \pi F \frac{\pi e^2}{mc^2} \lambda^2_{0v'} f_{xn} q_{0v'} \qquad (3\text{-}6),$$

where πF is the solar flux, λ is the wavelength of the incident radiation, f_{xn} is the oscillator strength for the transitions from the ground state to n', and $q_{0v'}$ is the Franck-Condon factor for the v=0 ground state to v' level.

The fractional population of a molecular state, $N(n'v'J')/N(n'v')$, is determined by the excitation process. Calculations of this ratio, applicable to NO spectra, may be found in Tatum (1967).

Finally, the transition probability $A_{J'J''}$ can be related to $A_{v'v''}$ using the Honl-London factors $S(J'J'')$. Then, $A_{J'J''}$ is expressed as

$$A_{J'J''} = A_{v'v''} \frac{S(J'J'')}{2(J'+1)} \qquad (3\text{-}7),$$

where 2(J'+1) is a normalization factor. The Honl London factors give the probability of a transition from an upper state J' to a lower state J''.

With

$$\omega_{v'v''} = \frac{A_{v'v''}}{\sum_{v''} A_{v'v''}} \qquad (3\text{-}8),$$

Equation (3-5) can be rewritten as

$$E = P(n'v') \frac{N(n'v'J')}{N(n'v')} \omega_{v'v''} \frac{S(J'J'')}{2J+1} \qquad (3\text{-}9).$$

The single scattering albedo, $\omega_{v'v''}$, can be determined from the Franck-Condon factors (Barth, 1965).

E. SYNTHETIC SPECTRA

The elements described in this chapter can be used to generate synthetic spectra. The calculation for a molecular band requires that the emission rates must be determined for each rotational line in the band. The spectral region is divide into wavelength bins. As the lines are calculated, they are added to the appropriate bin. This process is repeated until all the contributions have been added. Algorithms for this were developed by Cleary (1985) and were used in the analysis described below.

IV. THE EXPERIMENT

A. INTRODUCTION

The experiment was launched from White Sands Missile Range at 1700 GMT on March 30, 1990 aboard a NASA Terrier Black Brant sounding rocket. The payload consisted of two instruments. One, a Naval Research Laboratory (NRL) spectrograph, was designed to observe O^+ emissions in the F_2 region of the ionosphere. The second instrument, the Naval Postgraduate School's (NPS) Middle Ultraviolet Spectrograph (MUSTANG), was designed to measure the emissions from NO, N_2, and N^+ in the D and E regions of the ionosphere. The MUSTANG experiment produced the data which is the subject of this thesis.

The sounding rocket reached an apogee of 320 kilometers, with altitude information provided by ground based radar tracking stations. During the flight, the rocket's attitude control system (ACS) maneuvered the payload to optimize the conditions for data collection for each experiment. For the MUSTANG experiment, this involved positioning the payload to view the horizon with a 90 degree observation-zenith angle (horizontal viewing) and a 90 degree solar-observation angle. Approaching apogee, the payload was maneuvered through 270 degrees so that it was pointing at the zenith for part of the downward portion of the flight. At approximately 200 kilometers, the payload was again rotated to point towards the horizon. This positioning resulted in two sets of useable data from MUSTANG. On the up leg of the flight, spectra were recorded in the altitude range

16

of 150 to 200 kilometers. On the down leg, spectra were measured from 180 to 100 kilometers.

B. THE INSTRUMENT

The MUSTANG instrument is a 1/8 meter Ebert-Fastie spectrograph with an off axis telescope. The optical design is shown schematically in Figure 4-1. The entrance slit
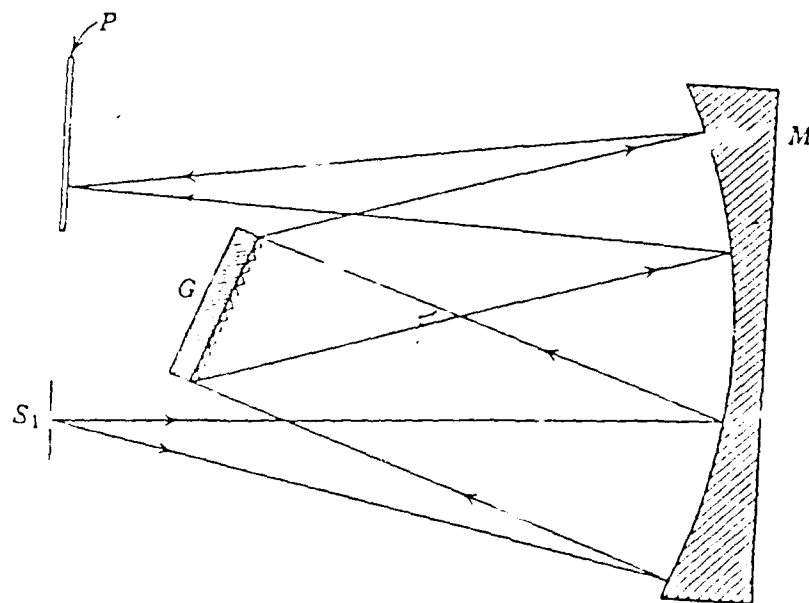

Figure 4-1 Optical Design of Spectrograph (from Samson, 1967)

17

was 5 millimeters in height by 140 microns wide producing a field of view of 2.3 degrees in the vertical and 0.006 degrees horizontal. The grating ruling was 1200 lines per millimeter. It's position was adjusted to produce a wavelength coverage of 1800 Å to 3400 Å. The detector system consists of an ITT F4145 microchannel plate image intensifier fiber optically coupled to a Hamamatsu S2300-512Q 512 element linear photodiode array.

The image intensifier is composed of a photocathode, two microchannel plates in cascade, and an output phosphor screen. The photocathode was placed in the focal plane of the spectrograph. Light from the mirror strikes the photocathode, causing an electron to be ejected. Electrical potentials across the image intensifier accelerate the electron through the microchannel plates (MCP). Figure 4-2 shows a block diagram of the device. The microchannel plates are similar to photomultiplier tubes in that 15,000 electrons are produced as output for every one input. These electrons exit the MCP and strike the phosphor, producing photons. The image intensifier fiber optic output window is in contact with the fiber optic input window of the photodiode array, resulting in negligible loss of photons The output of the photodiode is an analog voltage proportional to the incident intensity.

The wavelength calibration of the spectrograph was determined by identifying atomic lines from the spectra of platinum and mercury. The sensitivity of the instrument was determined by illuminating a barium sulfate ($BaSO_4$) screen using a standard deuterium lamp and a tungsten filament quartz-halogen lamp. At the time of this paper, the post flight calibration was not complete. As a result, the sensitivity calibration is still
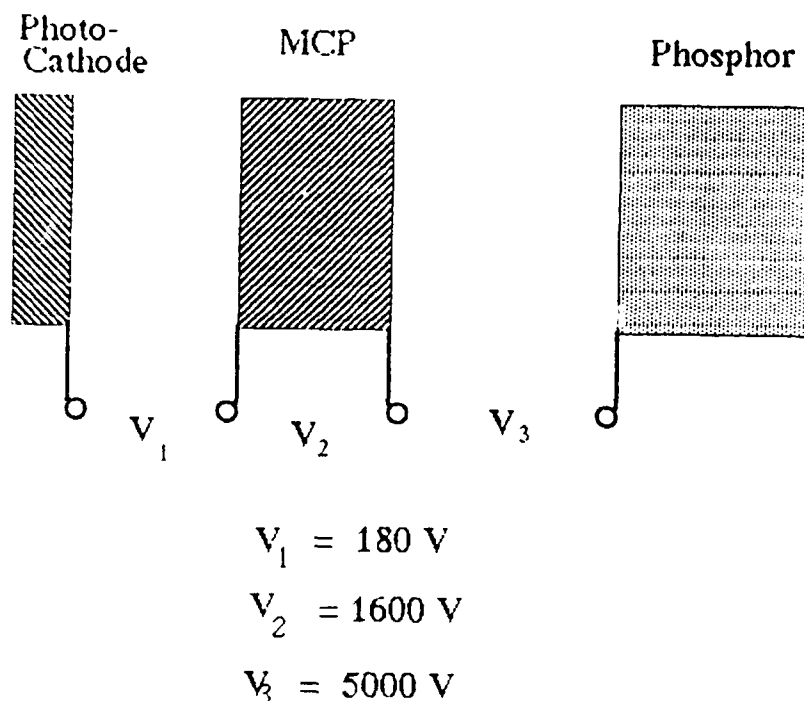
18

Photo-Cathode   MCP   Phosphor

V_1 = 180 V

V_2 = 1600 V

V_3 = 5000 V

Figure 4-2 Block Diagram of the Image Intensifier

preliminary. However, the systematic error introduced by the uncertainty in determining the sensitivity is typically 20% for these types of experiments (Cleary and Barth,1987; McCoy,1983). The detector response to an input was found to be linear up to 85% of its maximum output. Wavelength resolution of the instrument was found by determining the instrument slit function. This is simply the instrument response to a delta function input. The delta function was approximated by the atomic lines of mercury. Wavelength resolution was found to be 10.6 Å.

C.   THE OBSERVED SPECTRA

The observations are of the atmospheric dayglow under mid-day, mid-latitude conditions. The solar zenith angle was 62.9 degrees and the F10.7 was 186.9.

19

Data integration time was 50 milliseconds (ms). Output from the photodiode detector was converted into a stream of 512 ten bit digital words. These data were sent via telemtry to ground stations where they were recorded. The telemetry signal also carried mission elapsed time data, making it possible to correlate the spectral data with altitude information.

The spectra were averaged in ten kilometer bins. This resulted in an average of 100 spectra per altitude bin. The actual number of spectra in each bin varied by as much as 20% at the altitude extremes, due primarily to changes in the vertical velocity.

A total of 13 average spectra were obtained. Figures 4-3 through 4-5 are represensentative of the high, mid, and low altitude observations. Clearly seen are the nitric oxide emissions, particularly the $\gamma(1,0)$ transition at 2150 Å. The analysis of the following chapter concentrates on the NO emissions in the 2000 Å to 2500 Å range.
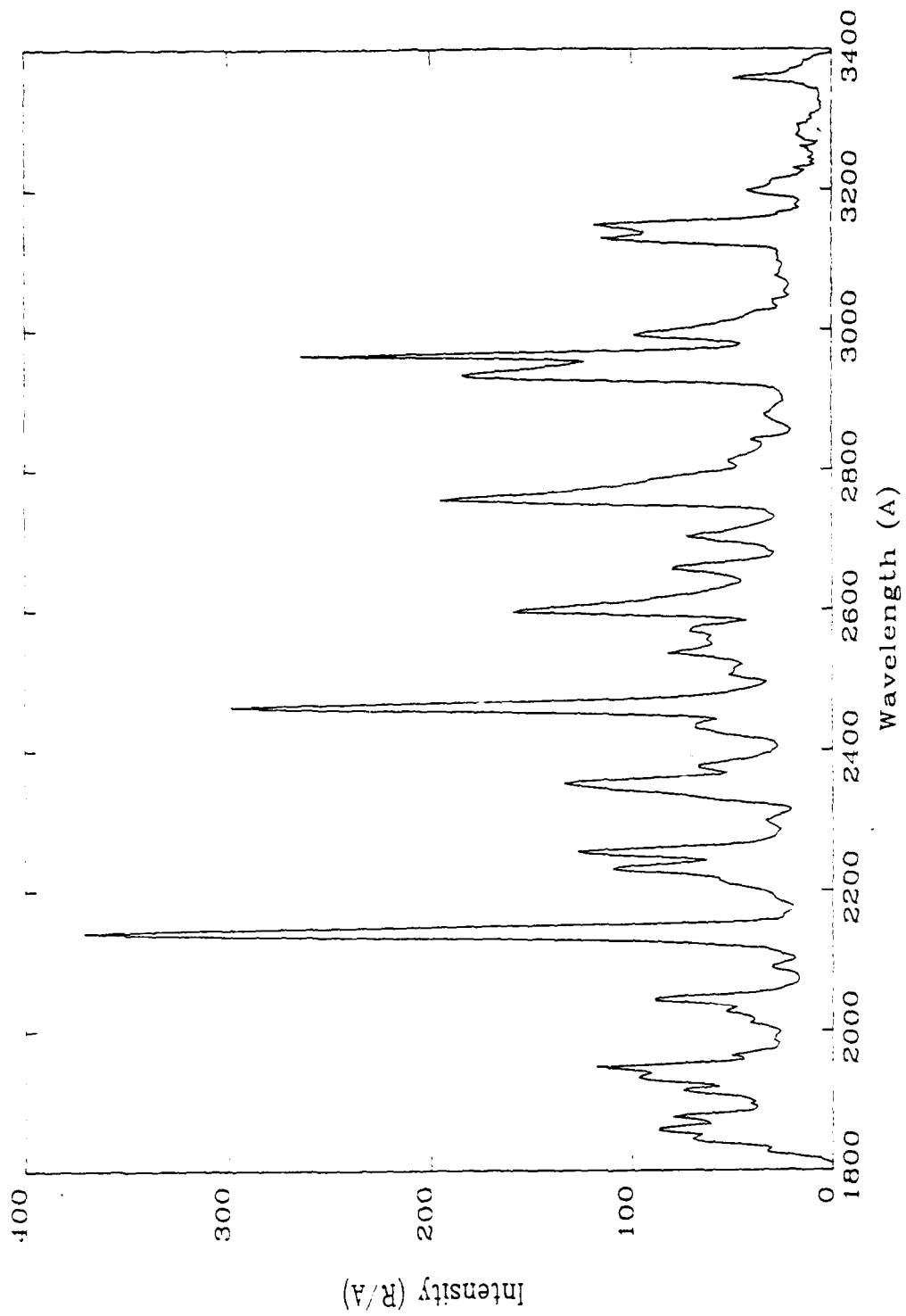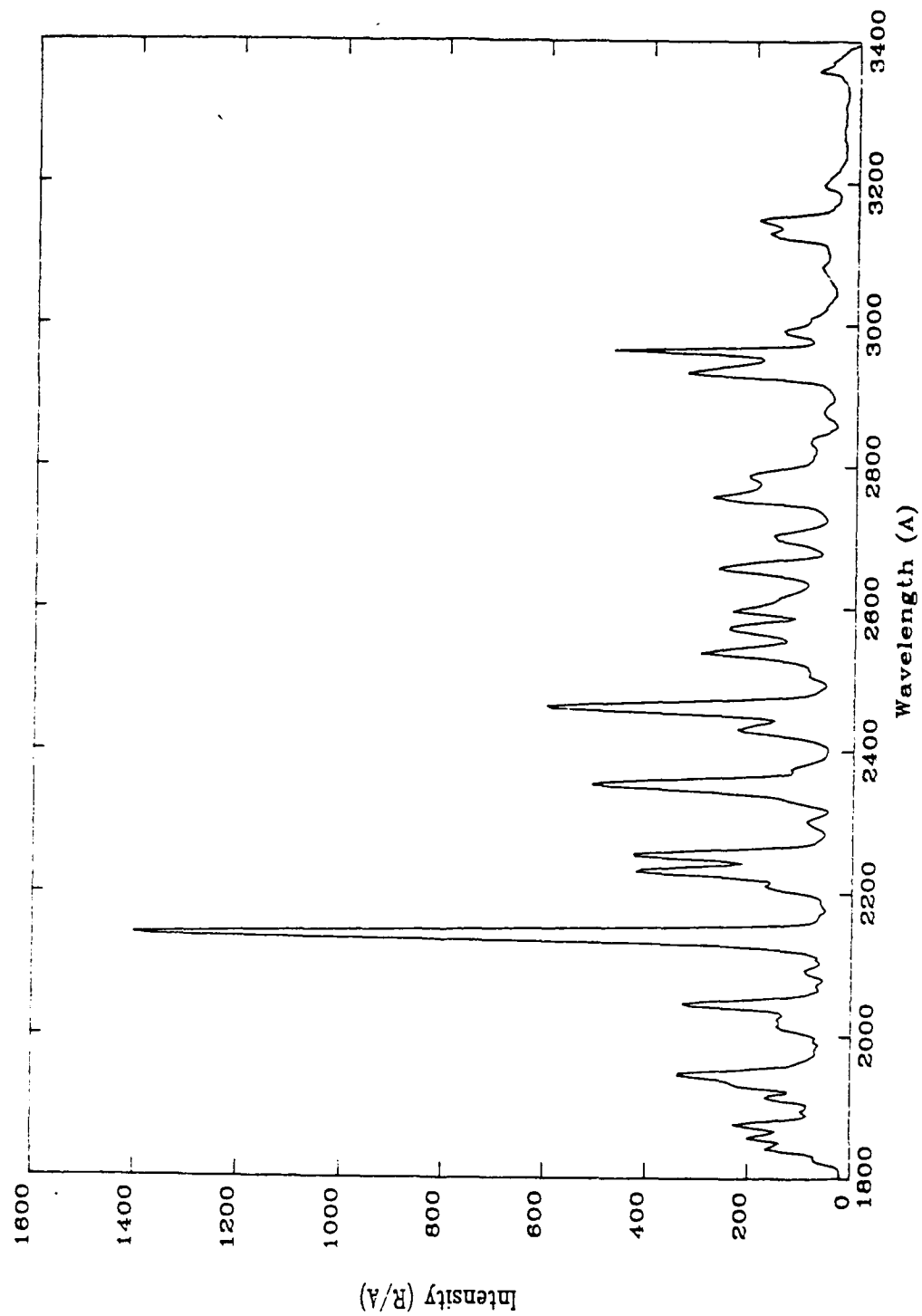
Figure 4-3 Spectrum at 195 km (Up Leg)

21

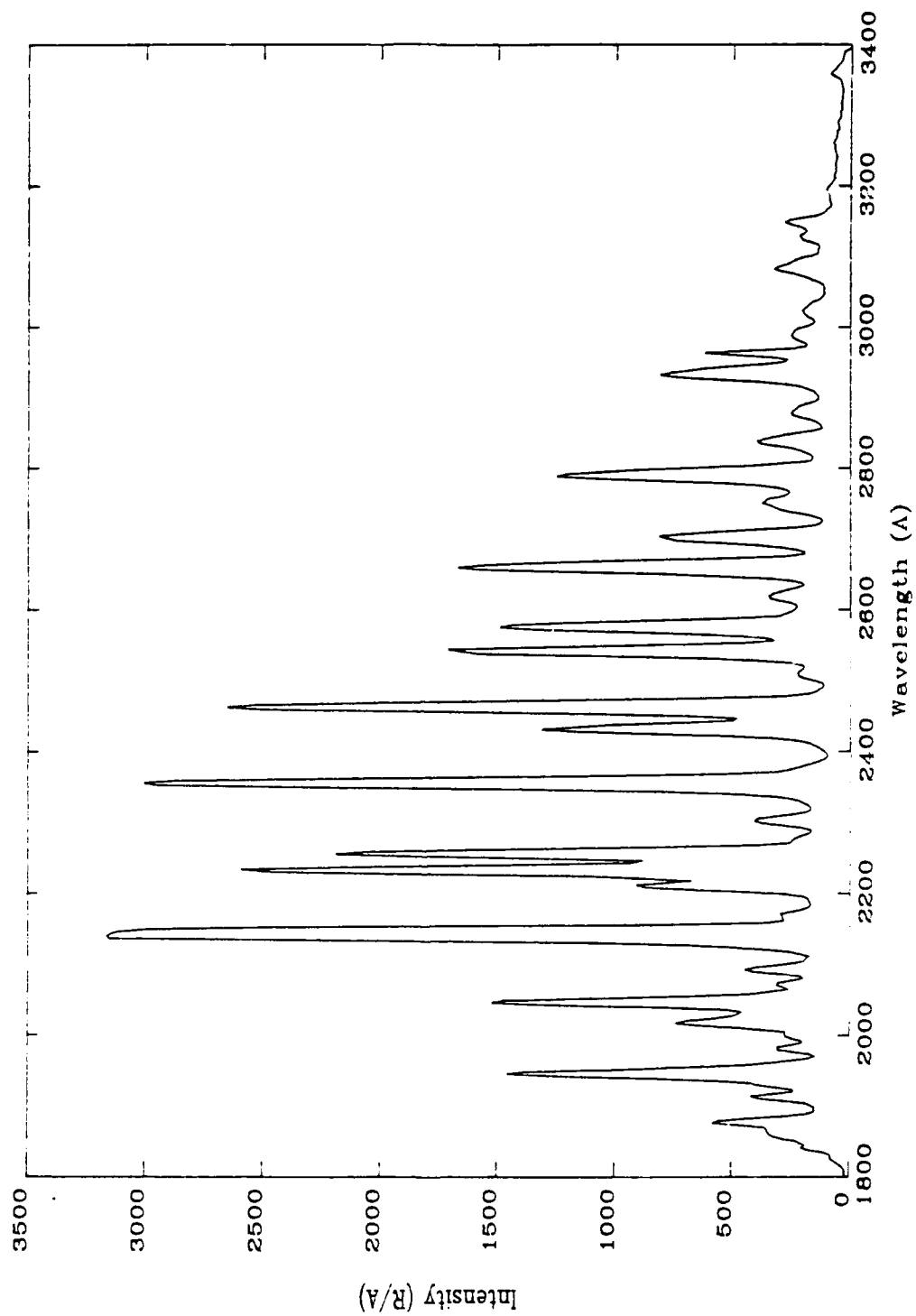**Figure 4-4** Spectrum at 155 km (Down Leg)

22

Figure 4-5 Spectrum at 105 km (Down Leg)

23

V. DATA ANALYSIS

A. INTRODUCTION

In this chapter, the data are analyzed by comparison with synthetically generated spectra. Eleven major features of the observed data are identified and fitted to the synthetically generated spectra by independently varying the corresponding synthetic nitric oxide emissions in the 2000 Å to 2500 Å range. The objective of the analysis is to extract NO line-of-sight column densities from the spectra. In addition, a temperature profile is obtained. Variations of the data from model predictions are explored and discussed.

The data readout from the instrument was dependent on telemetry clocks. During preflight preparations, it was discovered that the pulse width of one of the NASA timing signals did not meet specifications. This caused every seventeenth data word to be dropped from the telemetry stream. This was corrected during the data reduction by inserting an averaged value where the missing data should have been and shifting the adjacent subset of observed data points. An additional wavelength discrepancy was found when fitting the data with the synthetic spectra. The data appeared to be shifted progressively with increasing wavelengths. Figure 5-1 shows the wavelength shift as a function of band head wavelength. The low altitude spectra were used to determine the size of the shift. The postflight calibration is still in progress. As a result, it cannot be determined at this time whether this shift is an instrumental artifact or an actual

24

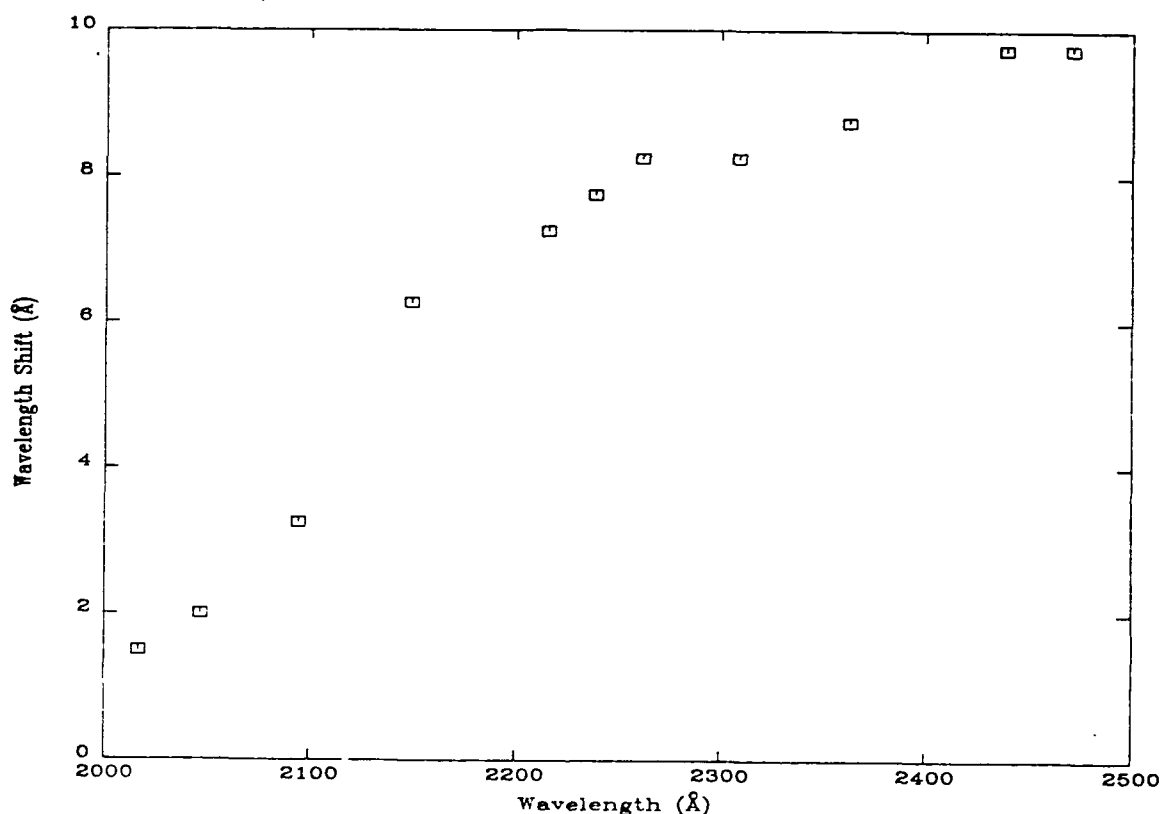disagreement between theory and data. During the fitting process, the data were shifted by the necessary amount.

Figure 5-1 Wavelength Shift Deduced From the Fit to the NO Bands

B. APPLICATION OF THE SYNTHETIC SPECTRA

The physical dimension of the synthetic spectra is an emission rate per atom per wavelength bin. The intensity of the observed data is in Rayleighs per Angstrom (one Rayleigh equals 10^6 photons cm^{-2} sec^{-1}). Thus, by fitting the data with the synthetic

spectra, one gets a scaling factor which can be directly converted to a column density. This method allows one to eliminate overlapping or contaminating emissions from the spectrum (Cleary, 1986). Though not pursued in this thesis, the resulting fit can be integrated over wavelength to get a column emission rate for any specific transition. In addition, the fit can be converted to a volume density through standard inversion techniques.

Before the synthetic spectrum was fit to the data, it was conditioned to model the response of the instrument. This involved convolving the synthetic spectra with the instrument slit function. As noted above, the instrument function was found by examining spectral lines of atomic mercury. Figure 5-2 shows the effect of this convolution.

The 11 NO emissions identified and fit are shown in Figure 5-3. The synthetic spectrum in this figure is a summation of the gamma and epsilon bands. Even with the low instrument resolution, the individual peaks are still distinct and relatively uncontaminated by other bands. A model of the NII 2143 doublet (not shown) is also included in the fit of the peak at 2150 Å.

Not all 11 features are fit at every altitude. At low altitudes, the stronger emissions saturate the detector. At higher altitudes, the molecular nitrogen Vegard Kaplan (VK) and Lyman-Birge-Hopfield (LBH) bands tend to obscure the weaker nitric oxide emissions. This was determined (to some extent) by fitting the data. These effects will be discussed later.
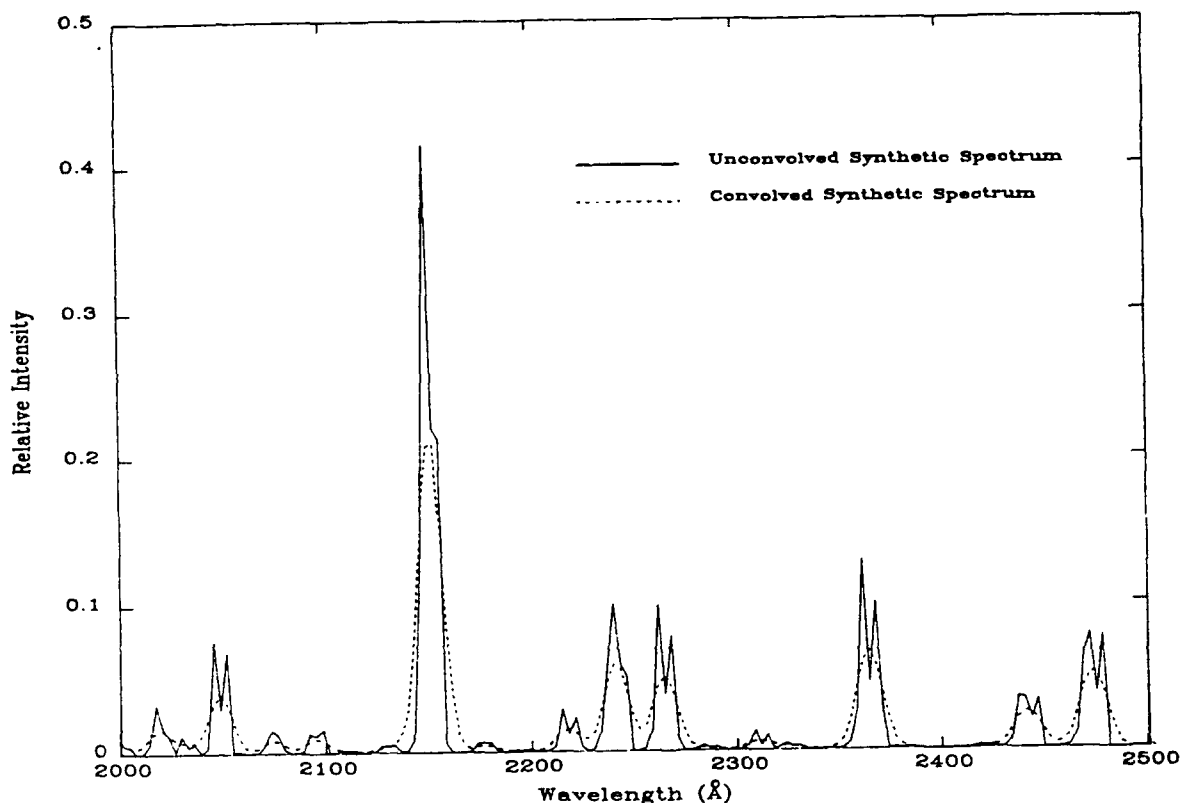
Figure 5-2 Representative Convolved Synthetic Spectrum

C. TEMPERATURE FITTING

Temperature was determined by matching the shape of the synthetic $\gamma(1,0)$ band to that of the data. There are several factors which complicate this process. For example, the intensity recorded by the instrument is a line-of-sight column emission rate. In the spherical geometry of the atmosphere, one would expect contributions to the spectrum from higher altitude, higher temperature regions along the slant path. The effect is small for an exponential atmosphere, but results in some smoothing of the spectrum from higher temperature contributions (see e.g., Bosserman, 1989). Additionally, the wavelength
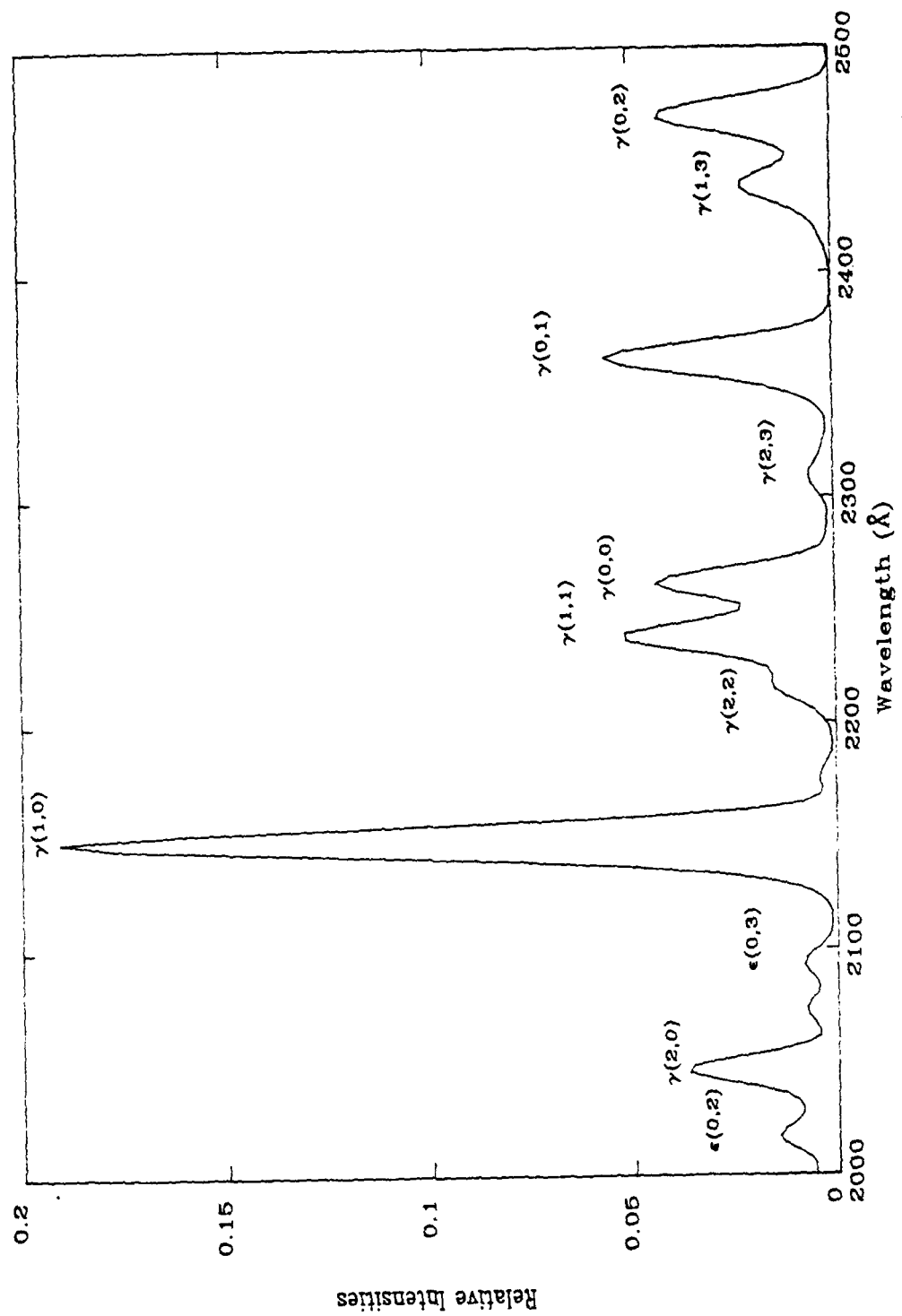
27

Figure 5-3 Nitric Oxide Synthetic Spectrum

28

resolution of the instrument is such that the rotational structure of a band is lost. Therefore, the sensitivity of the shape of a given band to changes in temperature is low. Because of this, the uncertainty in determining a temperature fit was taken as 100 K. The net effect of this uncertainty is to introduce a four percent systematic error into the inferred column densities.

Because of the instrument resolution, the NO (1,0) gamma band is blended with the $N^+(^5S)$ doublet at 2143 $\mathring{A}$. For mid-latitude observations at high altitudes, the NII doublet intensity is comparable to that of the NO gamma (1,0) band (Cleary and Barth, 1987). Therefore, it must be included in the fit. The contribution from the NII emission was modeled by two delta functions at 2143.6 $\mathring{A}$ and 3139.7 $\mathring{A}$ with an intensity ratio of 100:58 (Buscela and Sharp, 1989). As with the NO synthetic spectrum, the NII model was convolved with the instrument function.

The intensities of NO $\gamma(1,0)$ and NII emissions were treated as independent parameters in the model. For a given temperature, these parameters were varied in a grid search. The synthetic spectrum was fit to the data so as to minimize the chi-squared deviations. The temperature used to generate the NO synthetic spectrum was then adjusted in 100 Kelvin steps until the minimum in this third parameter was found.

A temperature profile was determined for all altitudes on the up leg and altitudes through 145 km on the down leg. Below this, the NO gamma (1,0) feature saturated the detector. For the lower altitudes, the down leg temperature profile was extrapolated by comparison with the predictions of the MSIS-83 (Hedin, 1983) neutral atmosphere model. Results of the fit are shown in Figure 5-4. Temperatures from the data are higher than

29

those given by the MSIS-83 model, indicating higher solar activity than the F10.7 indicates. As discussed below, a high level of solar activity is supported by the large nitric oxide column densities observed. Both the up-leg and down-leg temperatures show the positive gradient characteristic of the thermosphere. The temperatures determined from the fit were used throughout the rest of the data analysis.
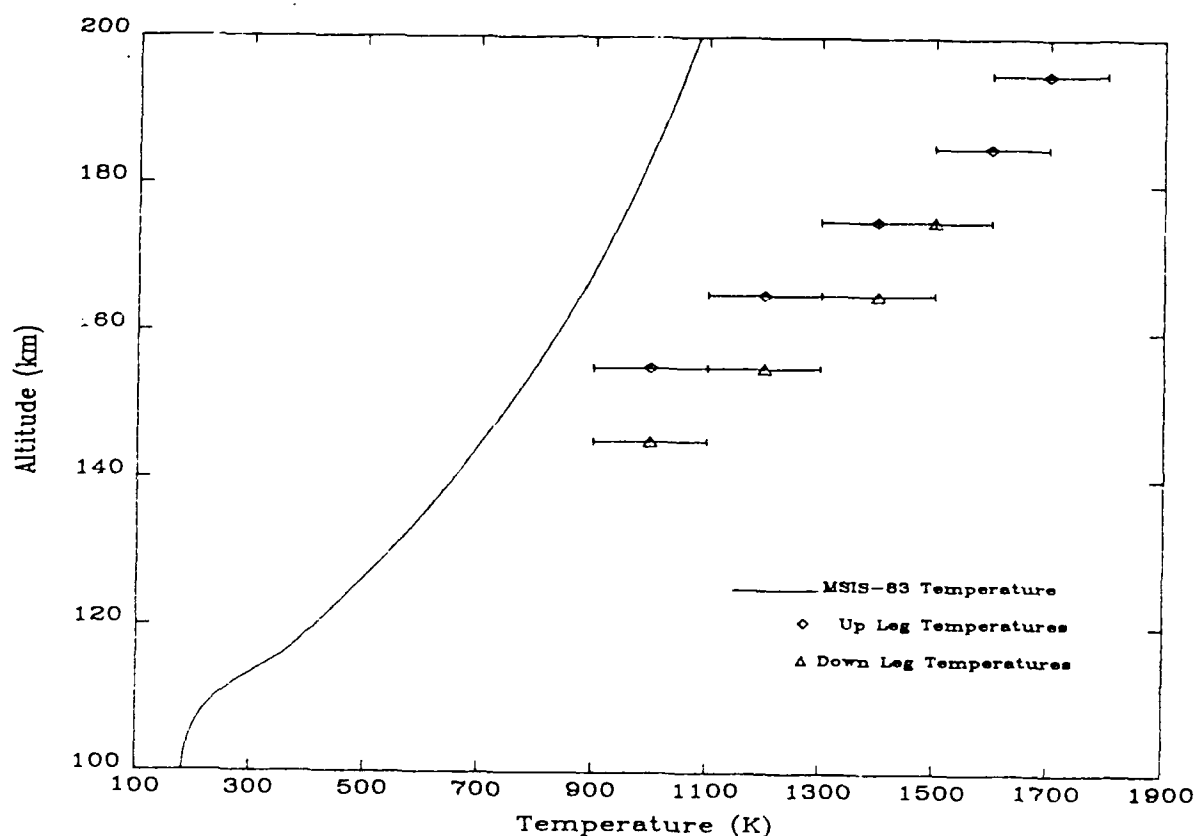

Figure 5-4 Temperature Comparison

D. FITTING THE DATA

Having determined the temperature profile using the $\gamma(1,0)$ band, the remaining ten emission features were fit with the synthetic spectra. Each synthetic spectrum was

30

multiplied by a scale factor to match the intensity of a specific emission. This scale factor is directly convertible to a line-of-sight column density. An average column density for a given altitude can be calculated from the estimated column densities that are determined for the individual peaks.

Not all the emissions were suitable for the fitting process at all altitudes. As with the NO gamma (1,0) band, the gamma (0,1), (0,2), and (1,1) bands saturated the detector at various altitudes below 145 km. In the higher altitude spectra, several of the NO bands are contaminated by emissions from the molecular nitrogen VK and LBH bands. The wavelength overlap of the NO and N_2 emissions is shown in Figure 5-5. Energetic electron impact is the principal excitation mechanism for the VK and LBH bands. The photoelectron flux is relatively low at the lower altitudes and increases with increasing height (over the altitude range considered here). Because of this, the intensity of the molecular nitrogen bands relative to the nitric oxide bands increases with altitude. The overlap of the the NO and N_2 bands can distort the shape of the NO emission spectrum, eliminating distinct features. Above 145 km, only the gamma (1,0), (2,0), and (1,1) bands were used in the fitting process.

The column densities are plotted by v'' progression for all 11 emissions in Figures 5-6 through 5-9. The data shown represent the down leg. Data from 185 km and 195 km on the up leg are included to indicate trends. It is instructive to note some of the features evident. For the gamma v'' band progressions in Figures 5-6, 5-7, and 5-8, there is a definite trend of increasing inferred column density with higher vibrational states. The relative intensities of emissions within a progression are controlled by the Franck-Condon
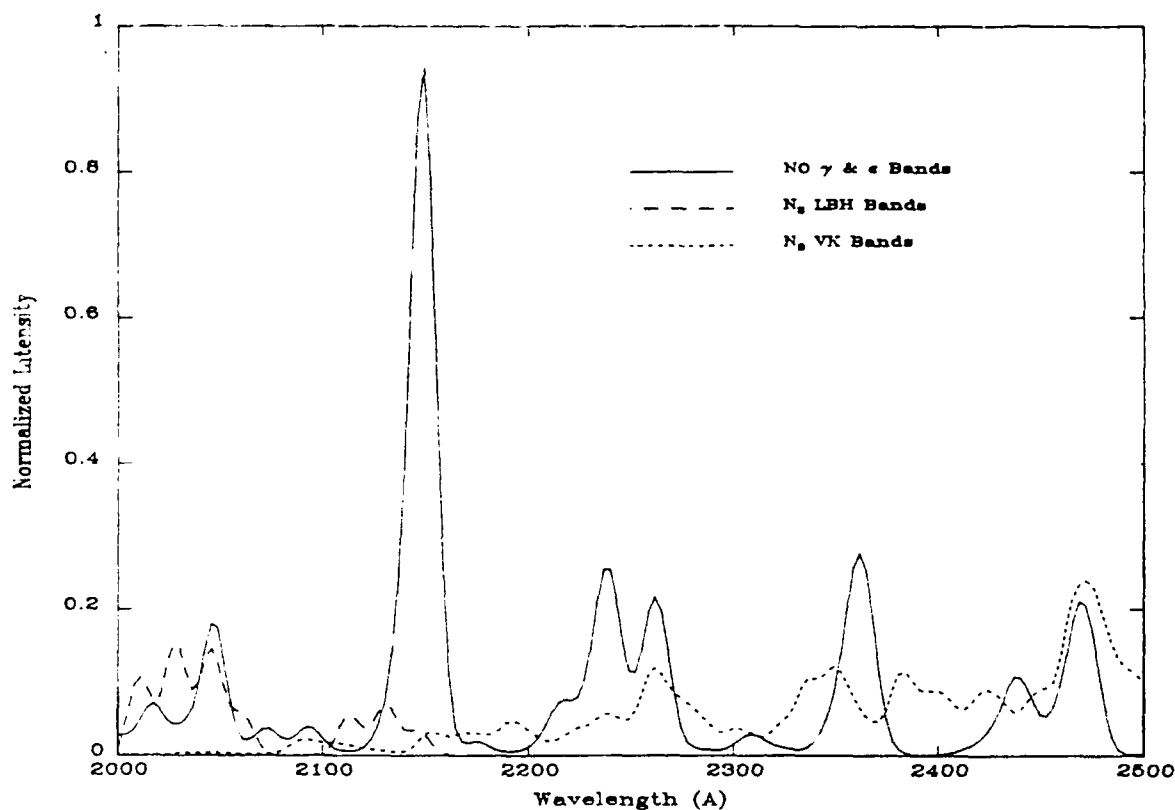
Figure 5-5 Wavelength Overlap of NO and N_2 Emission Bands

factors. Therefore, the scale factors (or column densities) yield a relative indication of the correctness of the Franck-Condon factors within a progression. If the Franck-Condon factors were in the correct proportions, one would expect the plots of the derived column densities to lie on top of one another. Instead, the data shows a systematic trend. Recently, Bosserman, (1989) showed a similar trend in the NO ϵ bands. He proposed corrections for the ϵ band Franck-Condon factors to bring his inferred column densities into agreement. The Franck-Condon factors for the $\epsilon(0,2)$ and $\epsilon(0,3)$ bands from Bosserman however, required little correction and the present work supports this (see
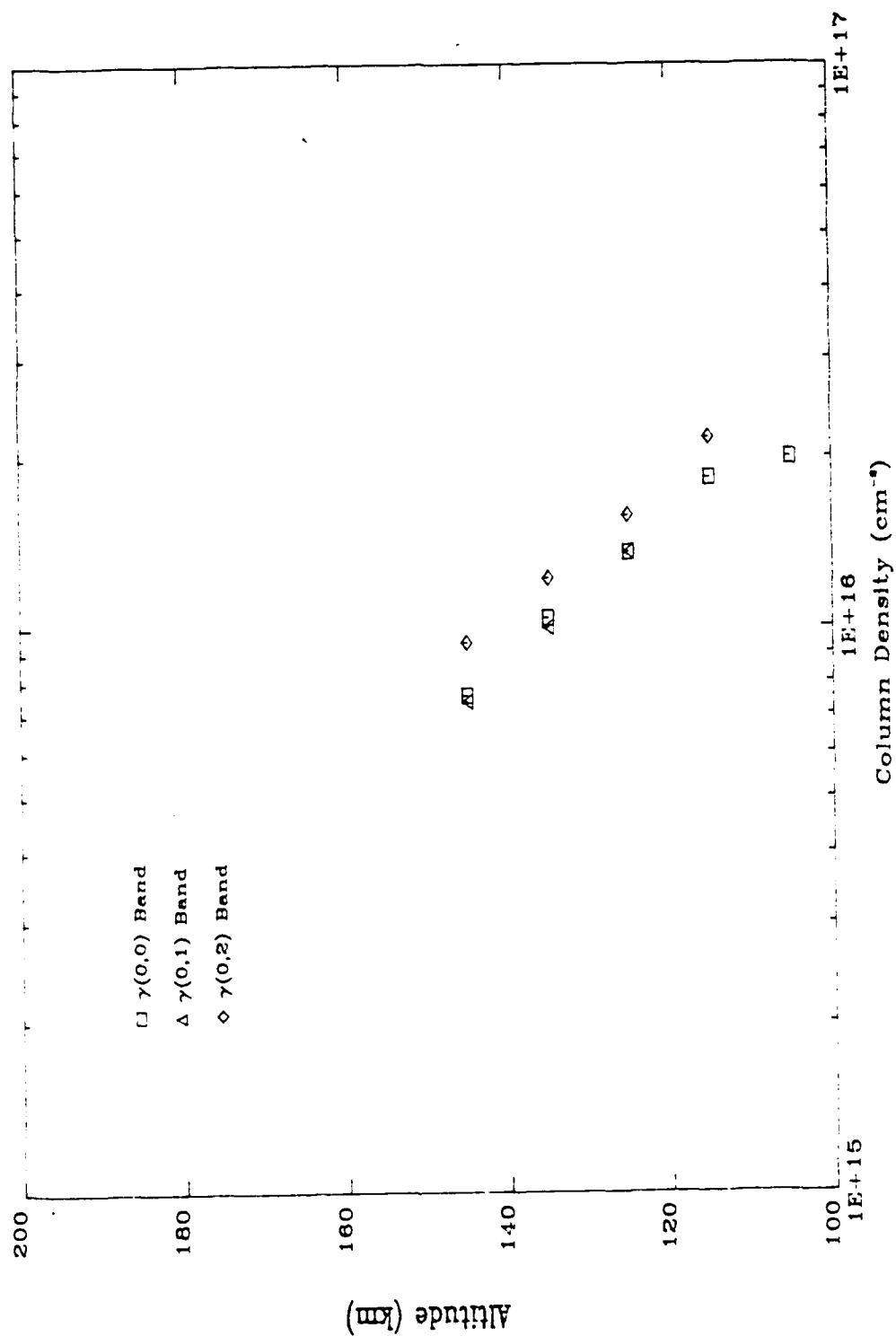
32

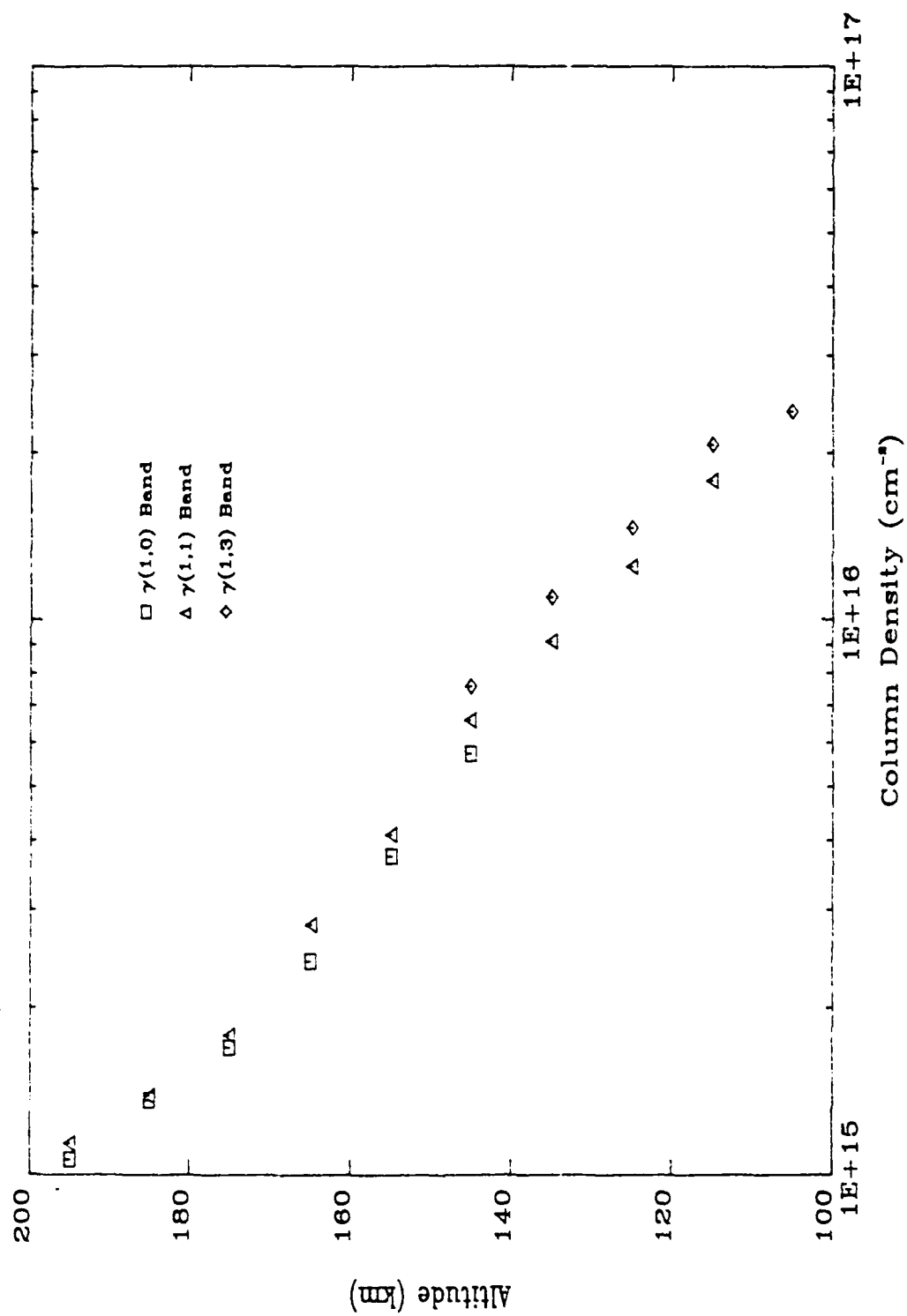**Figure 5-6** Column Densities for the γ (0,v″) Progression

33

Figure 5-7 Column Densities for the γ (1,v″) Progression
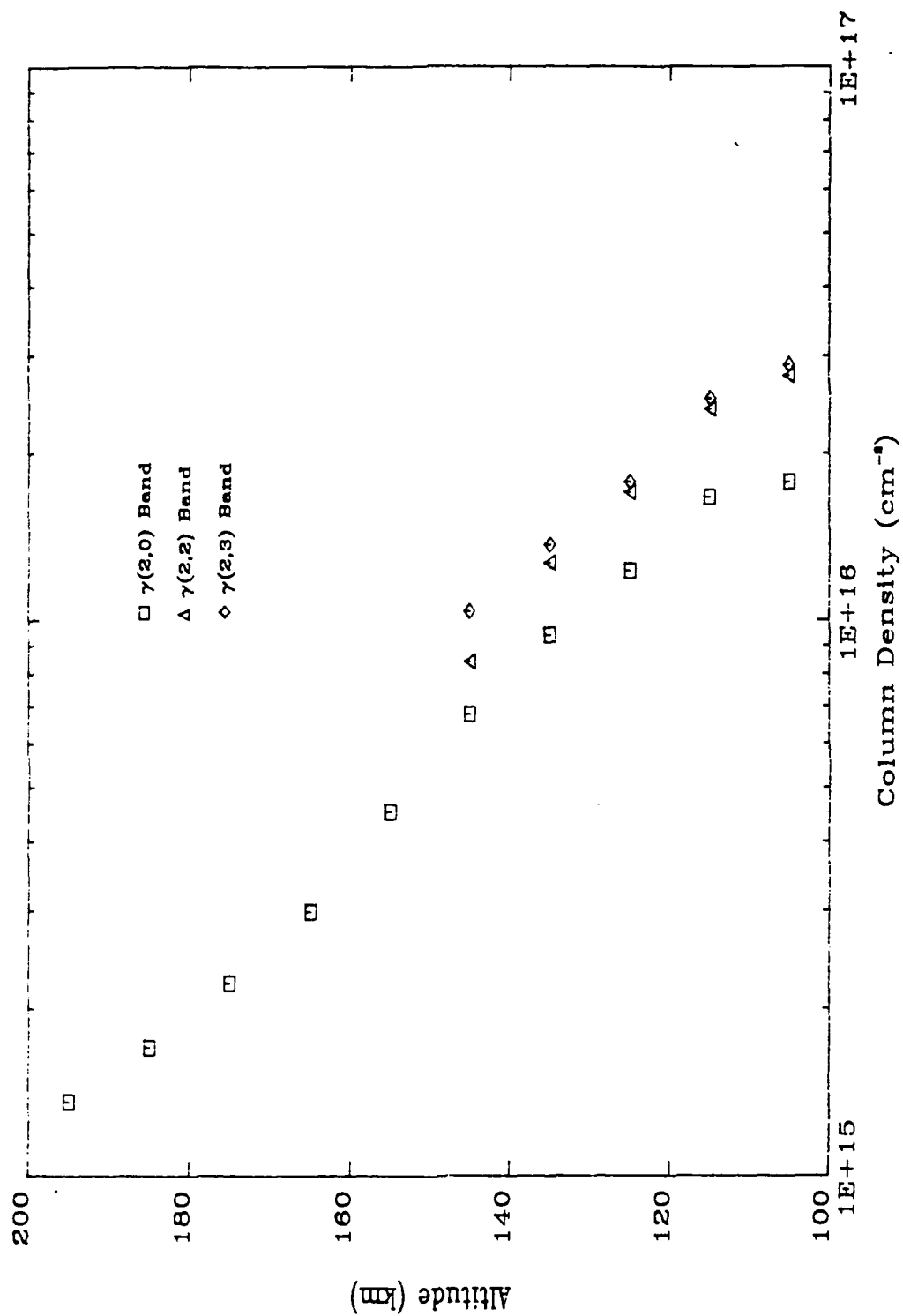
34

Figure 5-8 Column Densities for the $\gamma\ (2, v'')$ Progression
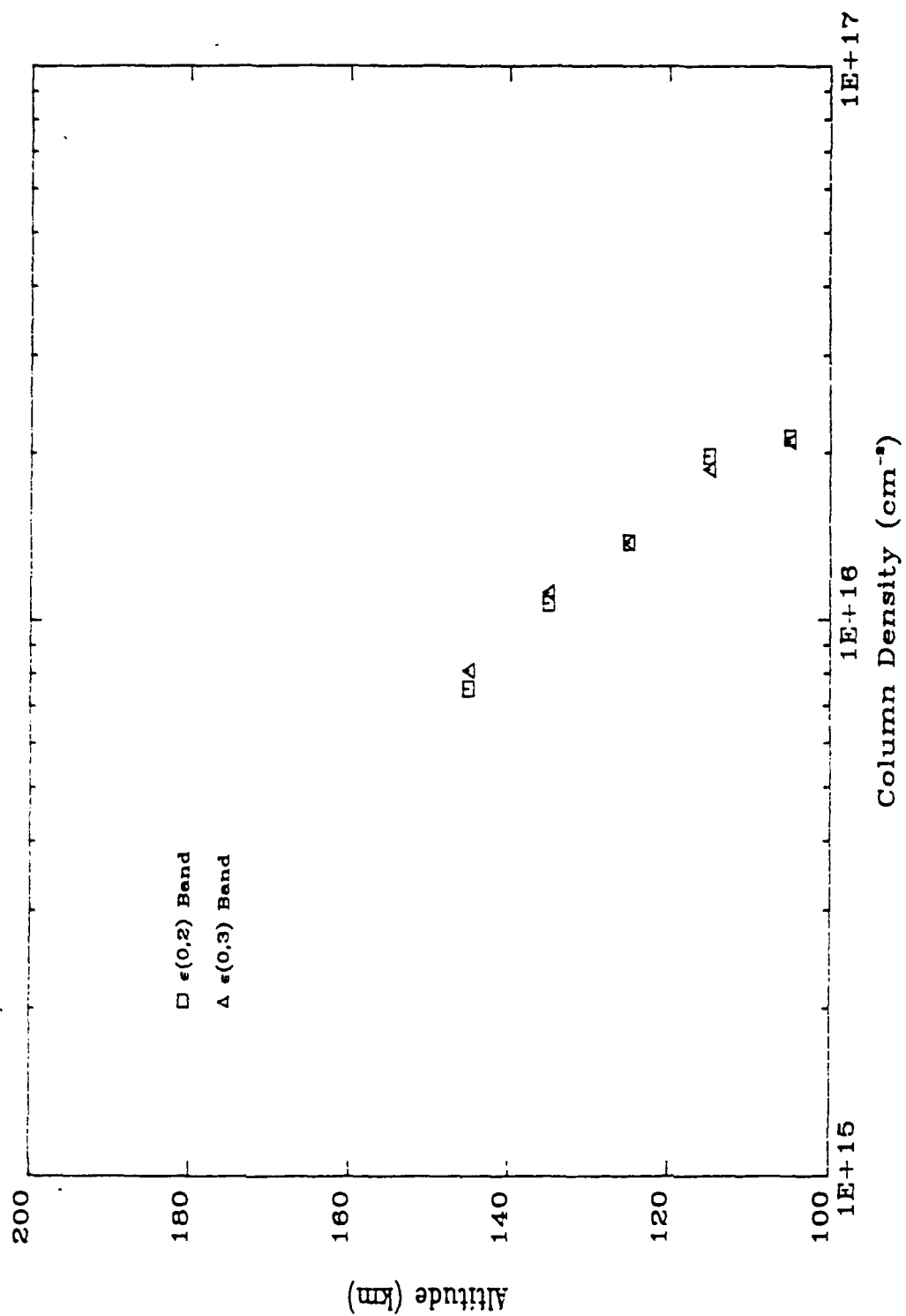
35

Figure 5-9 Column Densities for the $\varepsilon(0,v'')$ Progression

36

Figure 5-9). As a result, these two bands were used as a first guess for the average column density profile.

The ratios of the γ band column densities to this average column density yields a "Franck-Condon Scale Factor," as shown in Figure 5-10. These correction factors are averaged over all altitudes and are plotted against the band head wavelength for the emissions. This plot shows that while there is a trend in the Frank-Condon scaling factors within each progression, it is not purely wavelength dependent. Thus, it is unlikely to be due to some artifact of the sensitivity calibration of the instrument, but rather is a real physical effect.

A best fit column density profile can be obtained after correcting for these Franck-Condon scale factors. Figure 5-11 shows the results for the up- and down-leg. The error bars in Figure 5-11 are plotted as three times the uncertainty for purposes of clarity.

Figure 5-11 shows a difference of almost 30% between the up- and down-leg column densities at 155 km. The time between sets of data was approximately five minutes, therefore it is unlikely that temporal variations in atmospheric densities are the source of this discrepancy. The rocket's ACS data are still being analyzed, but differences in payload attitude may explain this feature of the spectral data. Because of this, the up-leg and down-leg spectra were treated separately in the analysis.

The column densities in Figure 5-11 are quite large for mid-latitude observations (see e.g., Cleary and Barth, 1986, McCoy, 1981). However, the Sun is approaching one of the strongest solar maxima recorded. The solar activity which drives the production of odd nitrogen has been, on the average, higher than normal. This fact makes these large
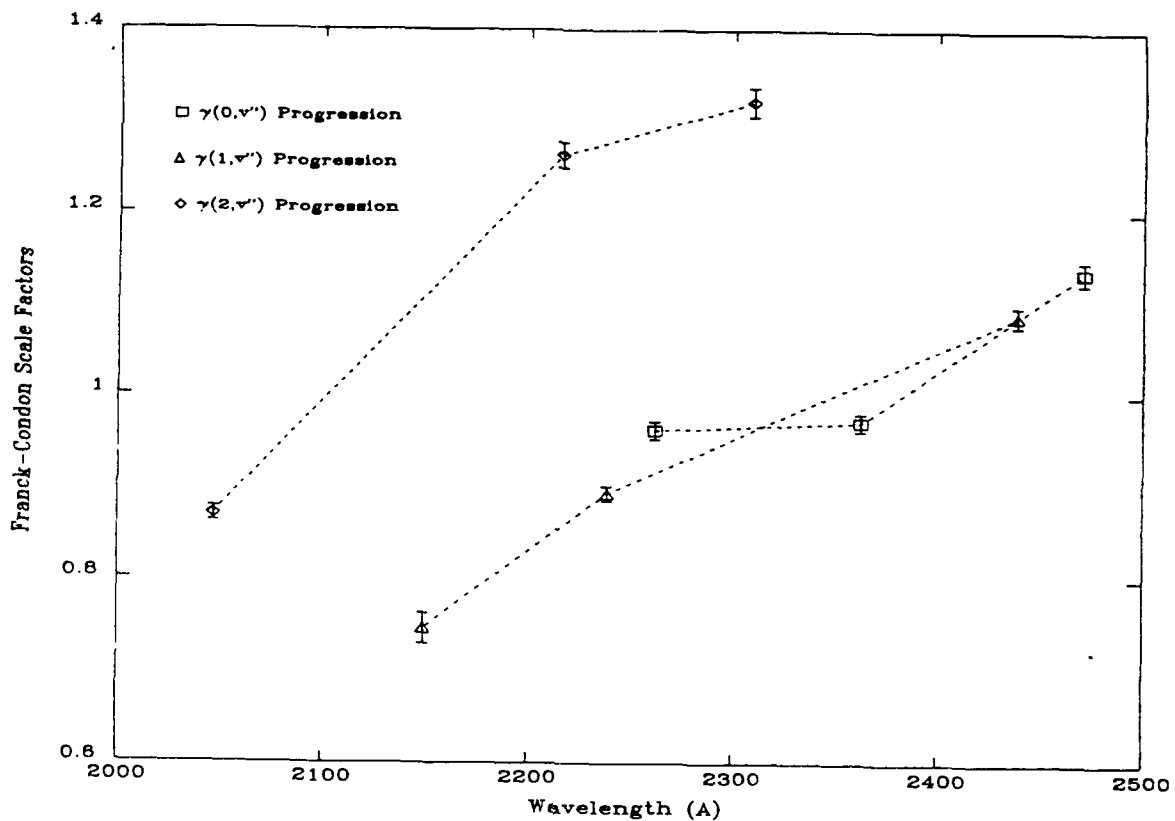
Figure 5-10 Franck-Condon Scale Factors

densities plausible. Each plot shows the characteristic exponential altitude dependence of the density. However, the upleg density falls off at a slower rate. In the plot of the downleg spectra, a peak near 105 km is quite evident.

Finally, Figures 5-12 through 5-24 show the best synthetic fit to the 13 averaged spectra. The synthetic fits have been corrected with the Franck-Condon scale factor adjustments while the wavelength adjustments shown in Figure 5-1 have been added to the data. The data are presented in the order of their acquisition; upleg spectra by increasing altitude and downleg spectra by decreasing altitude.
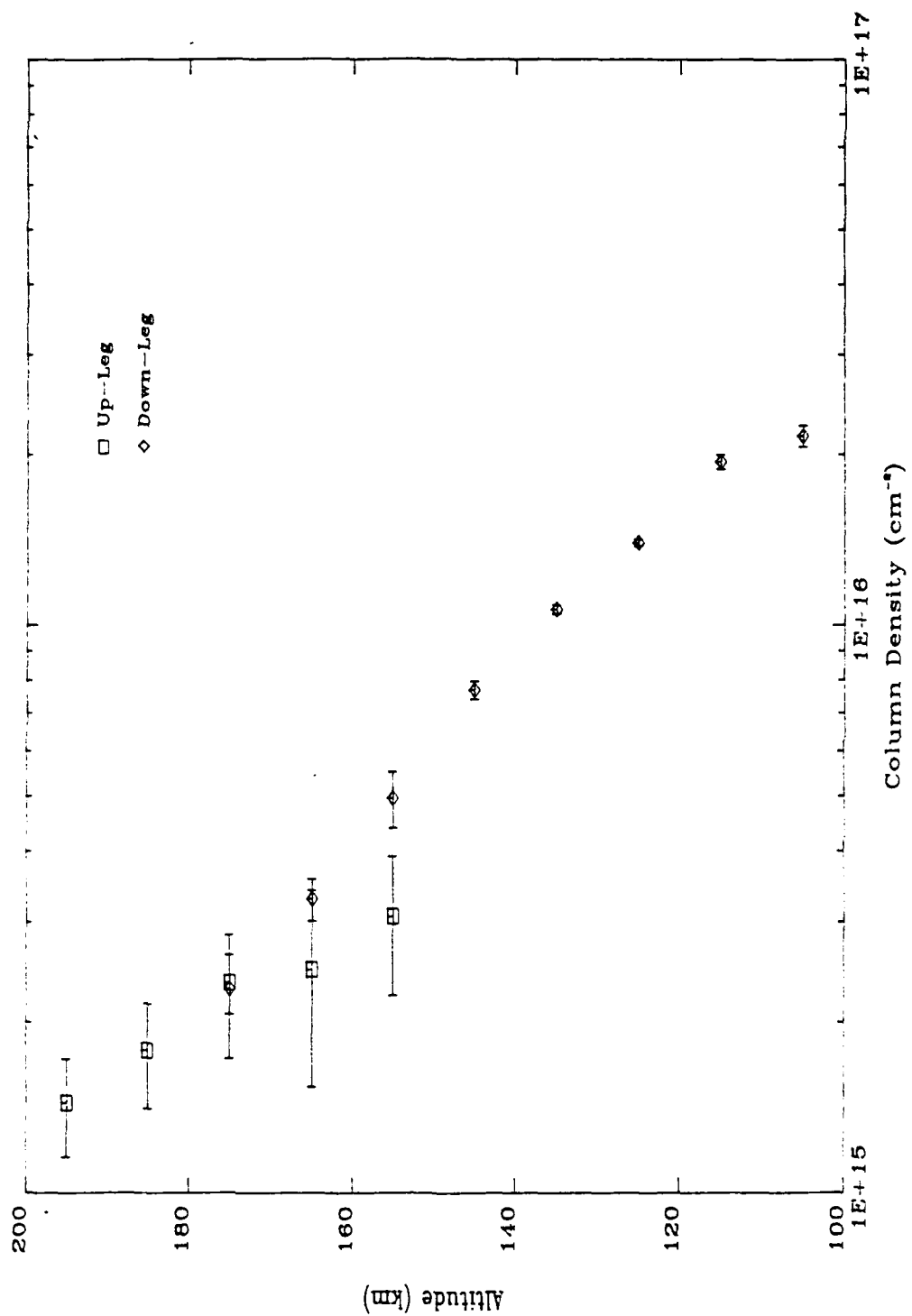
38

Figure 5-11 Average Column Densities

Adjusting the Franck-Condon factors for the various NO bands has clearly resulted in a good fit to the data. This is particularly evident at low altitudes where there is less contamination from other sources. At high altitudes, the contamination from the VK bands at long wavelengths is quite evident. In particular, the shoulders on either side of the $\gamma(0,1)$ peak near 2360 Å are due to the VK bands. The VK bands also add to the intensity of the $\gamma(0,0)$, $(0,2)$, and $(2,3)$ peaks near 2265 Å, 2310 Å, and 2475 Å respectively. At shorter wavelengths, between 2000 Å and 2100 Å, one can see the contributions from the LBH bands affect the shape of the $\gamma(2,0)$ peak and the two ε bands. What is not accounted for is the discrepancy between the observed $\gamma(1,0)$ peak and the synthetic spectrum from 145 km to 185 km on the up and down legs. The synthetic fit uses both the NO γ and ε bands and the NII emission at 2143 Å. There is some overlap of this peak with an LBH band, so this may account for some of the discrepancy.

In the low altitude fits, contamination of the spectrum by N_2 emissions is negligible. There are however, some features which stand out. One of these is the detector saturation in the $\gamma(1,0)$ band, seen in Figures 5-22 through 5-24. This causes the distortion of that peak. Additionally, at these low altitudes, one of the weaker NO emissions, the $\varepsilon(1,4)$ band, can be seen at 2073 Å. This emission feature was not fit with synthetic spectra. Below 125 km, the synthetic spectrum appears to over estimate the observed $\gamma(2,0)$ emission at 2050 Å. This may be due to self-absorption in the observed data, an effect which has been noted by other researchers (Cleary, 1986). Last, there is a divergence between the observed intensity of the $\gamma(1,1)$ band at 2240 Å and the synthetic fit. Above 135 km, the $\gamma(1,1)$ band synthetic spectra provides the best fit of all the emissions. Below

135 km, this changes. The synthetic band fits the data quite well on the long wavelength side of the peak, but the peak intensity and short wavelength fit show a marked difference. This suggests that the difference may be caused by another emission, though for now, it remains unexplained.
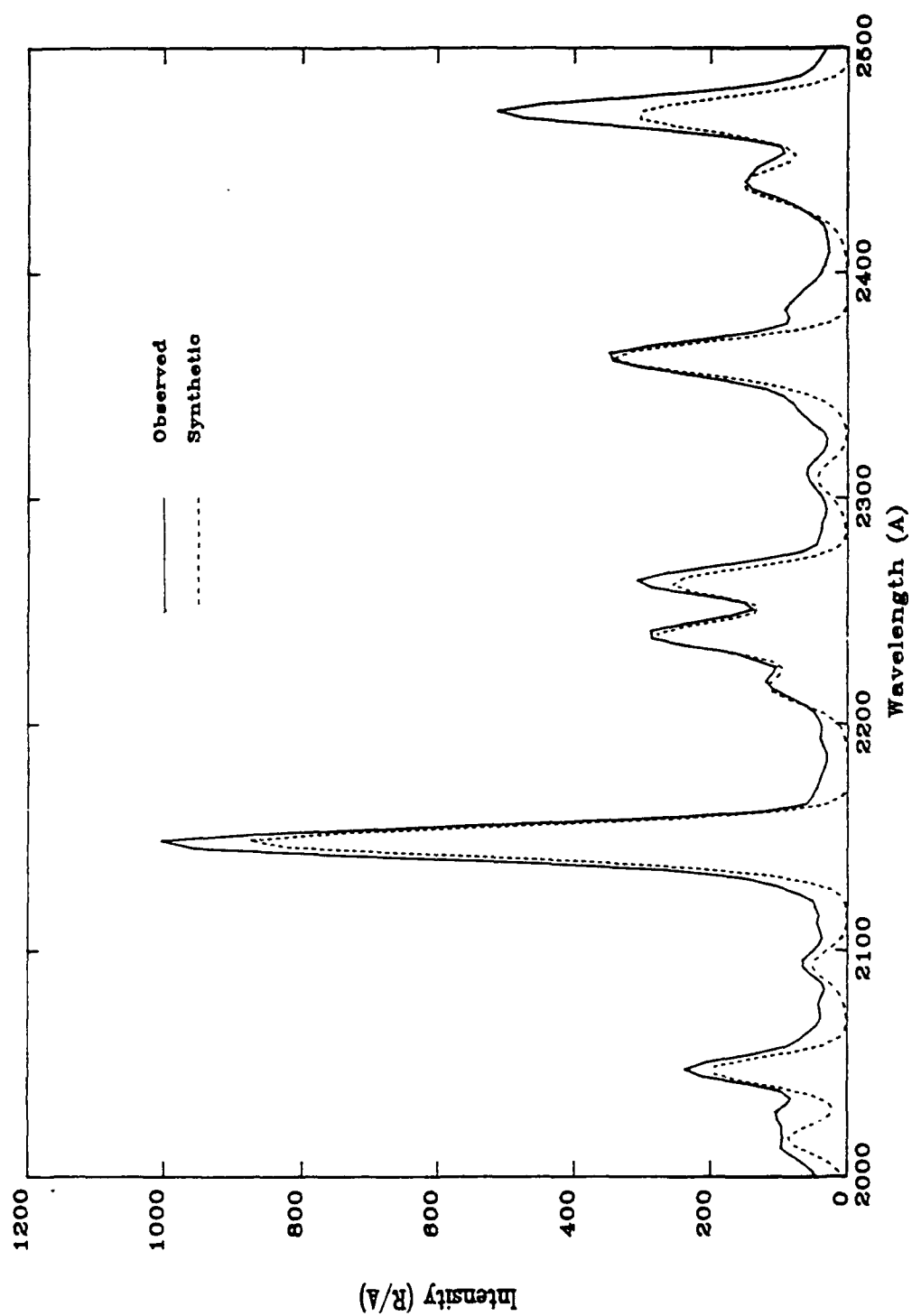
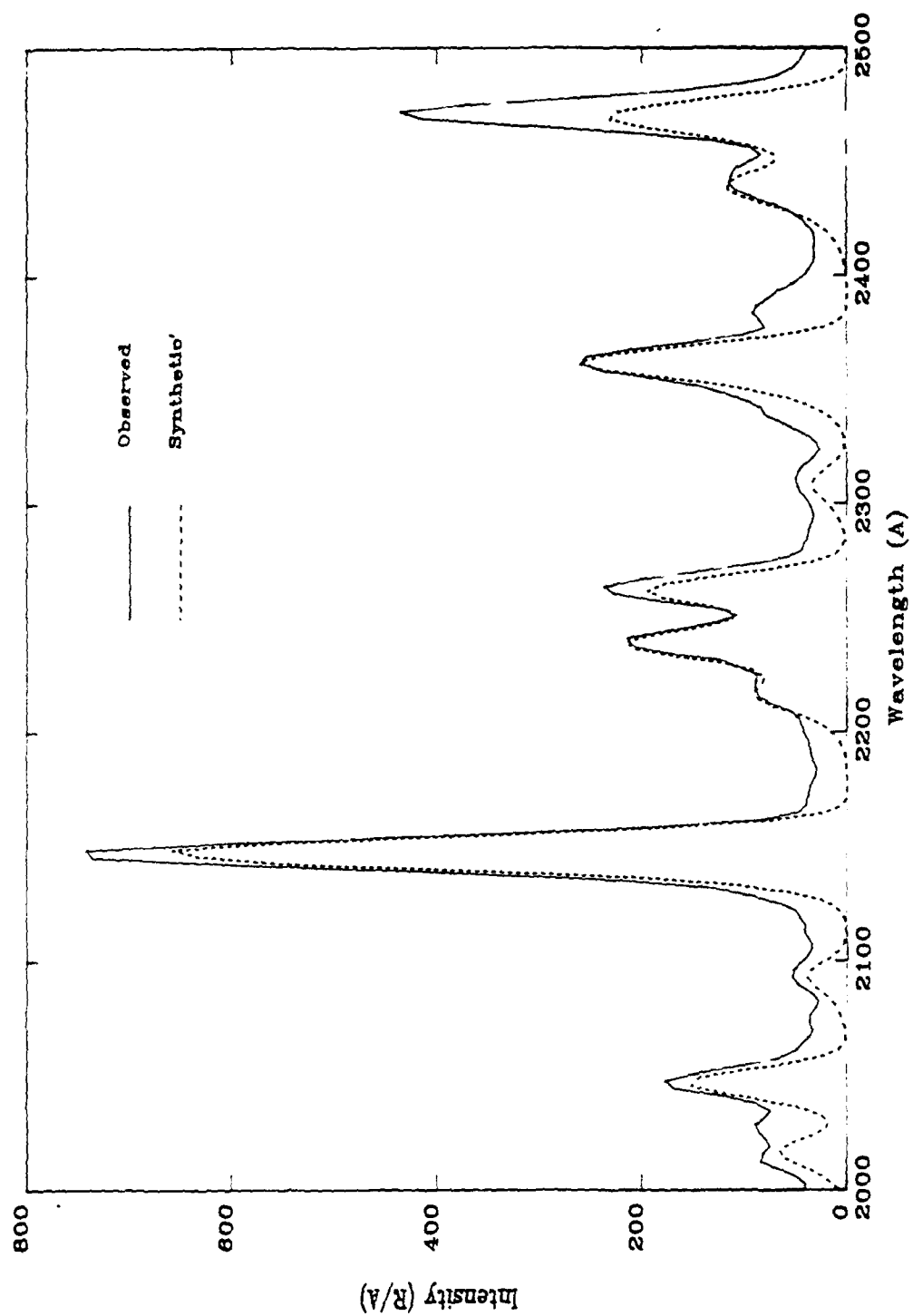**Figure 5-12** Comparison of Data and Synthetic Fit at 155 km (Up Leg)

42

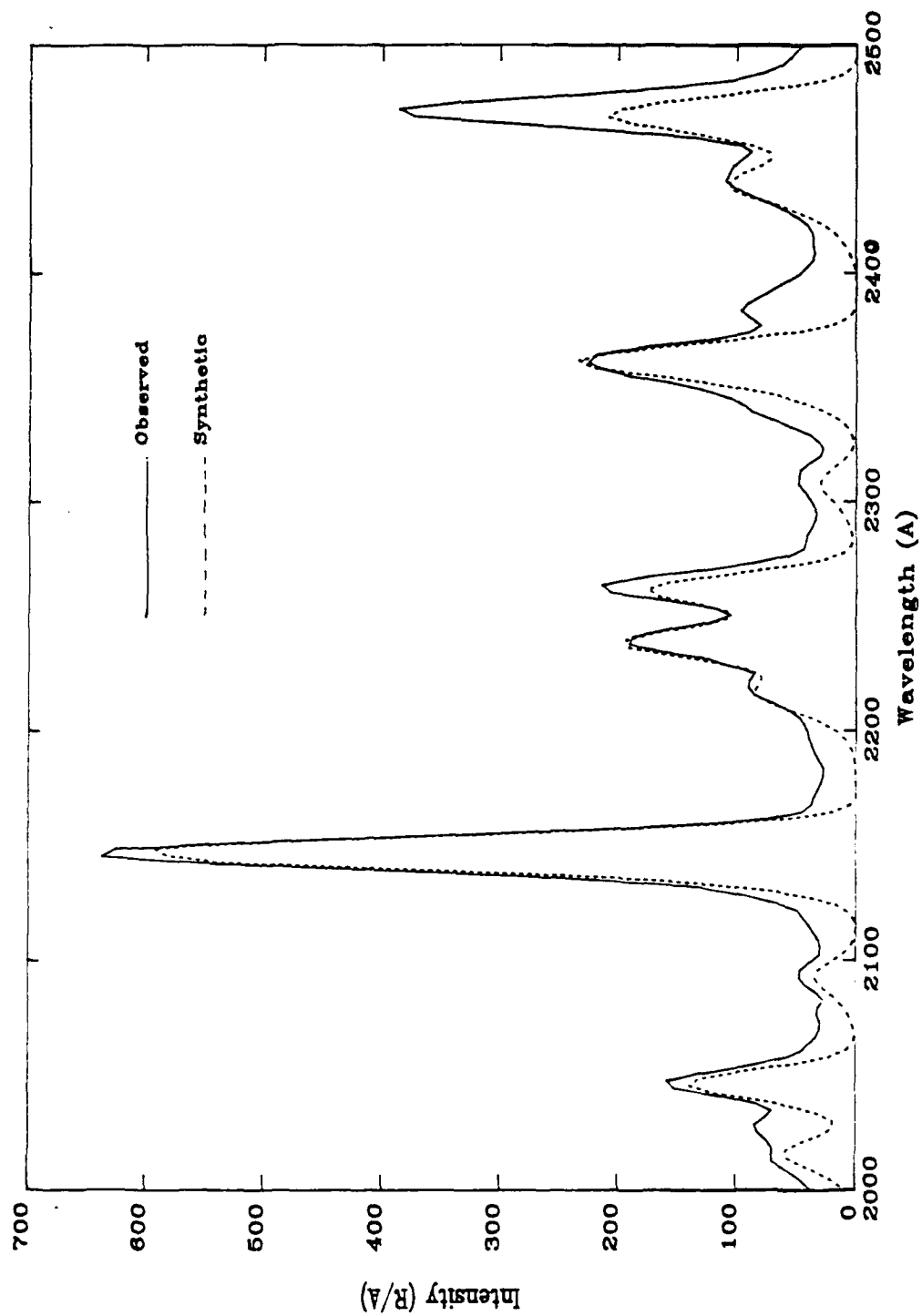**Figure 5-13** Comparison of Data and Synthetic Fit at 165 km (Up Leg)

43

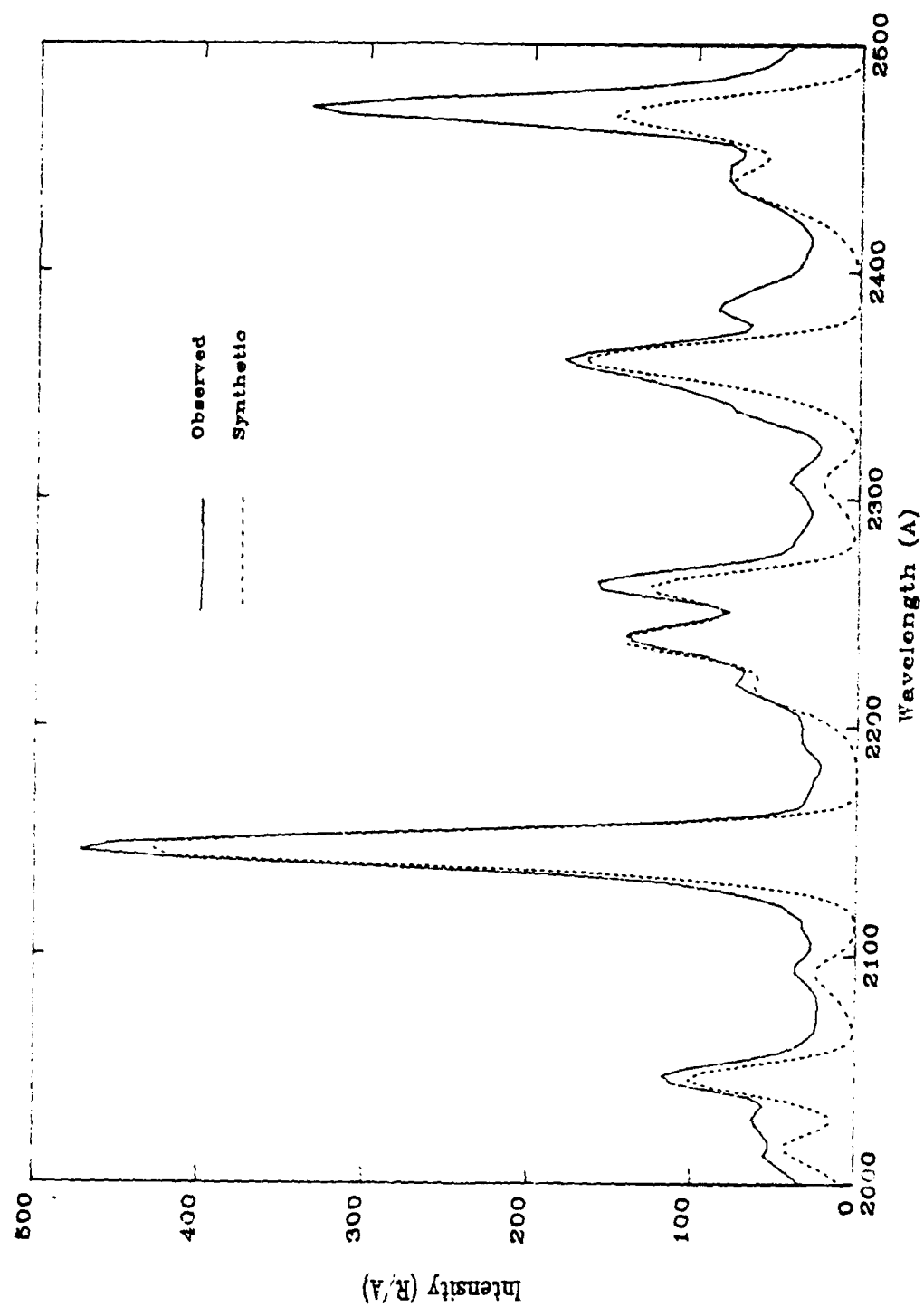**Figure 5-14** Comparison of Data and Synthetic Fit at 175 km (Up Leg)

44

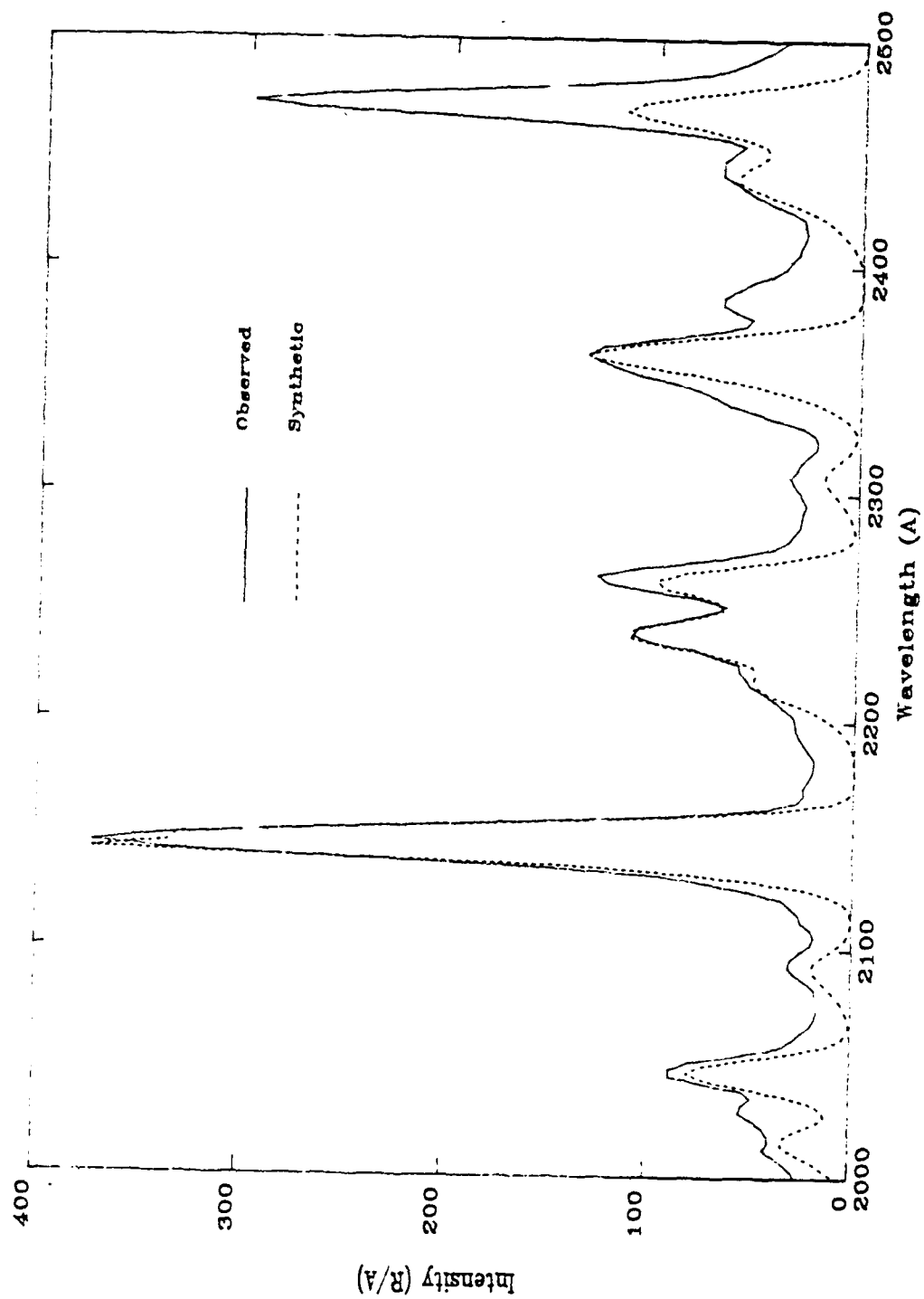**Figure 5-15** Comparison of Data and Synthetic Fit at 185 km (Up Leg)

15

Figure 5-16 Comparison of Data and Synthetic Fit at 195 km (Up Leg)

46

Figure 5-17 Comparison of Data and Synthetic Fit at 175 km (Down Leg)

47

Figure 5-18 Comparison of Data and Synthetic Fit at 165 km (Down Leg)

48

Figure 5-19 Comparison of Data and Synthetic Fit at 155 km (Down Leg)

49

Figure 5-20 Comparison of Data and Synthetic Fit at 145 km (Down Leg)

50

Figure 5-21 Comparison of Data and Synthetic Fit at 135 km (Down Leg)
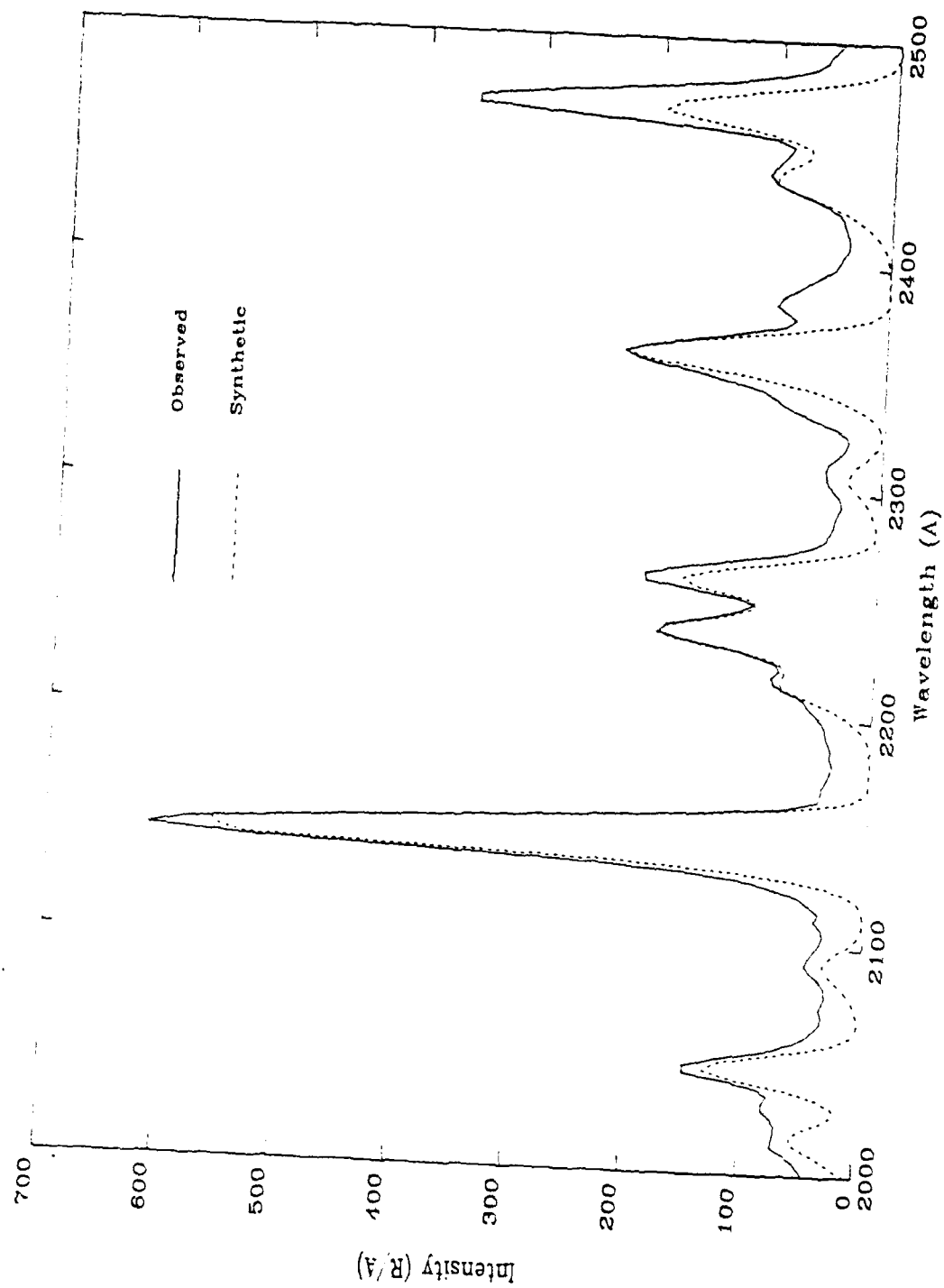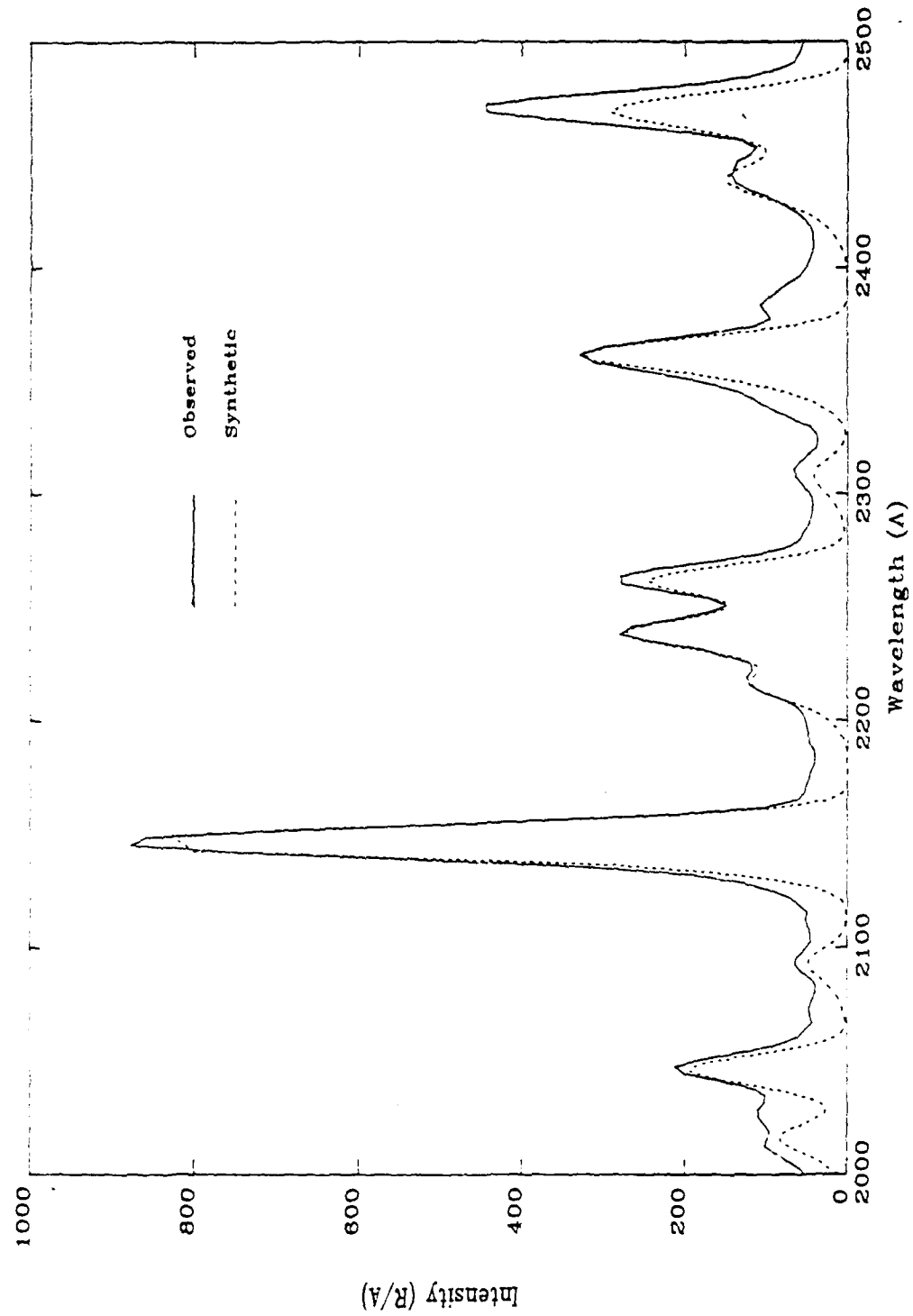
51

Figure 5-22 Comparison of Data and Synthetic Fit at 125 km (Down Leg)

52
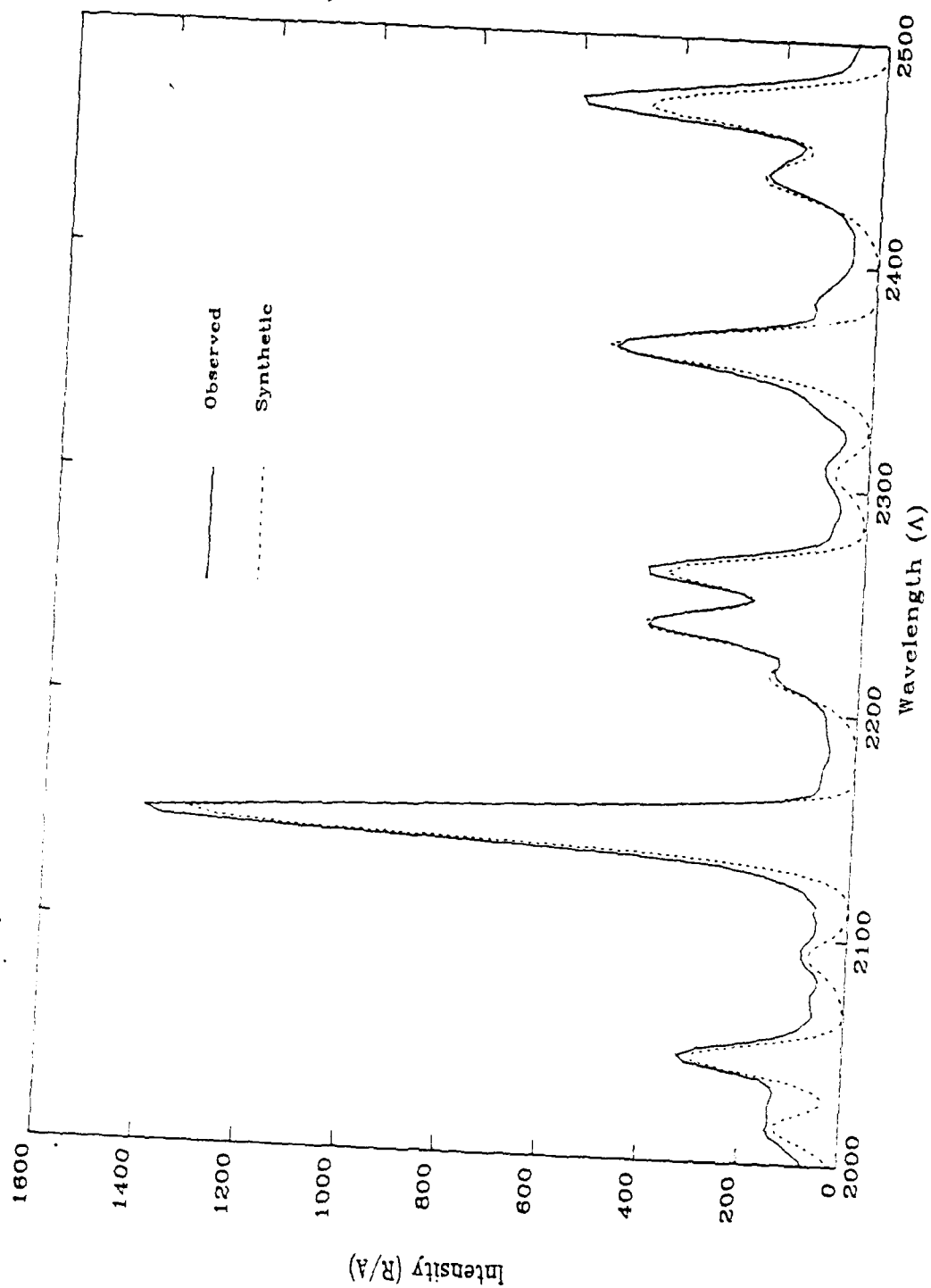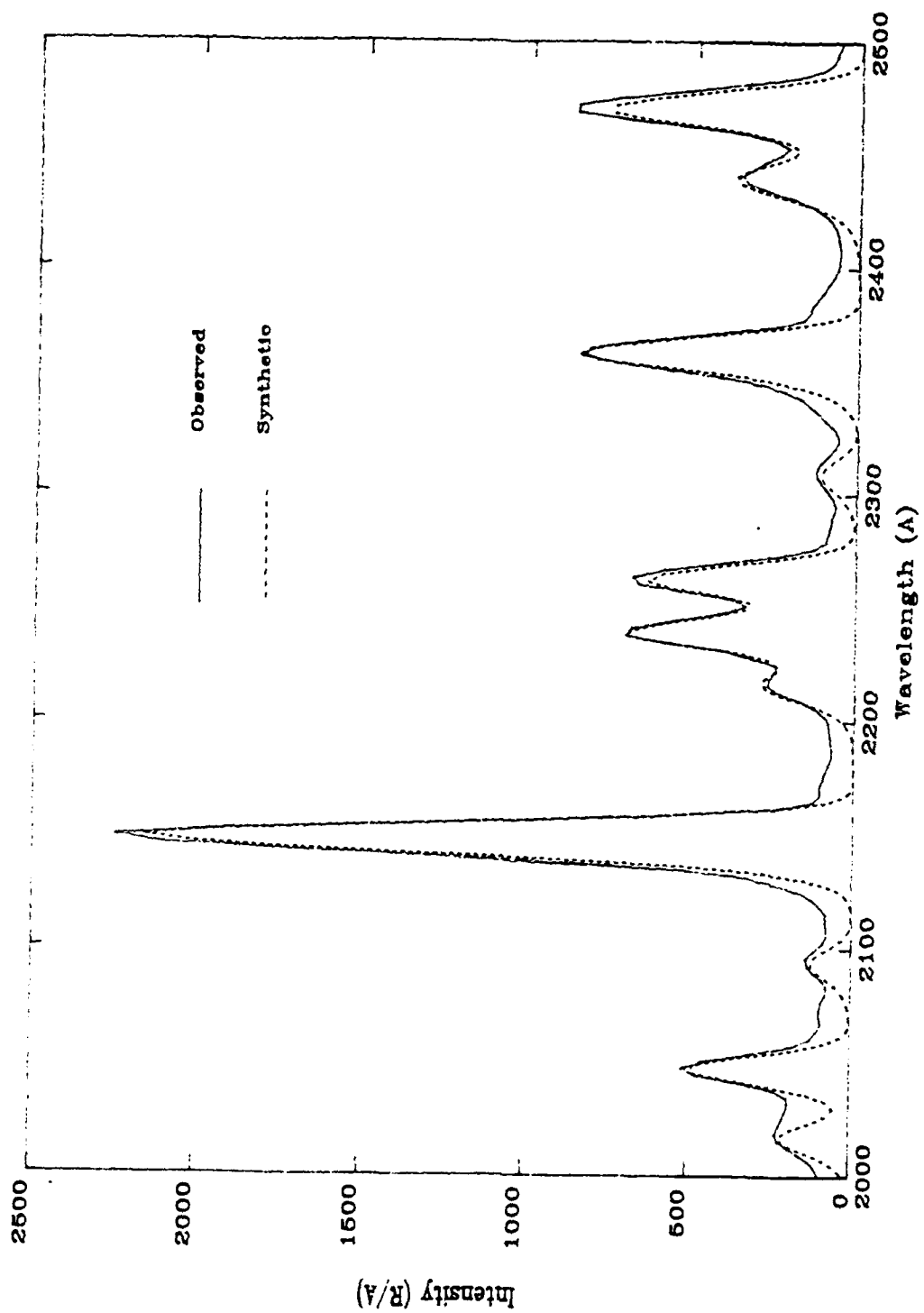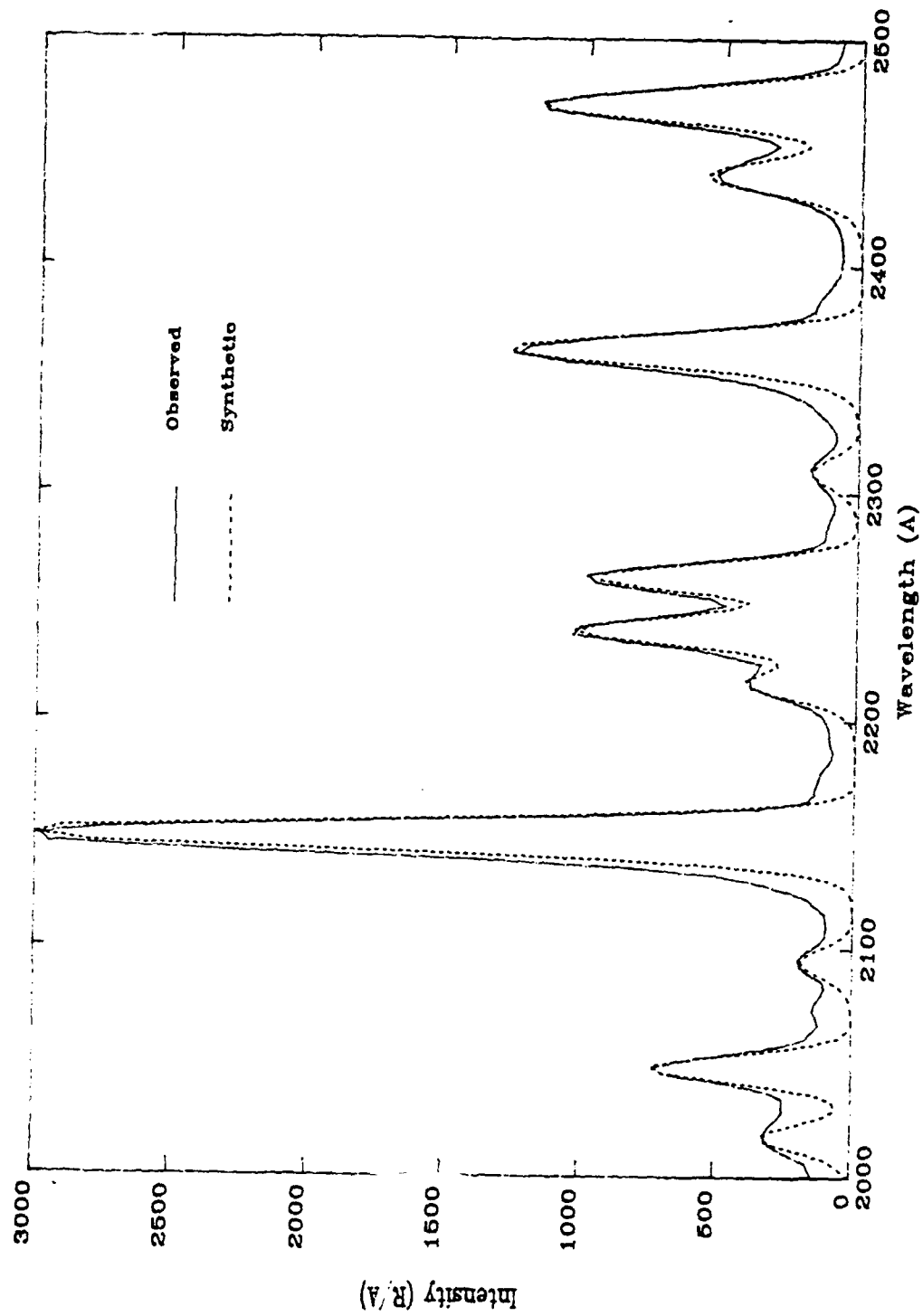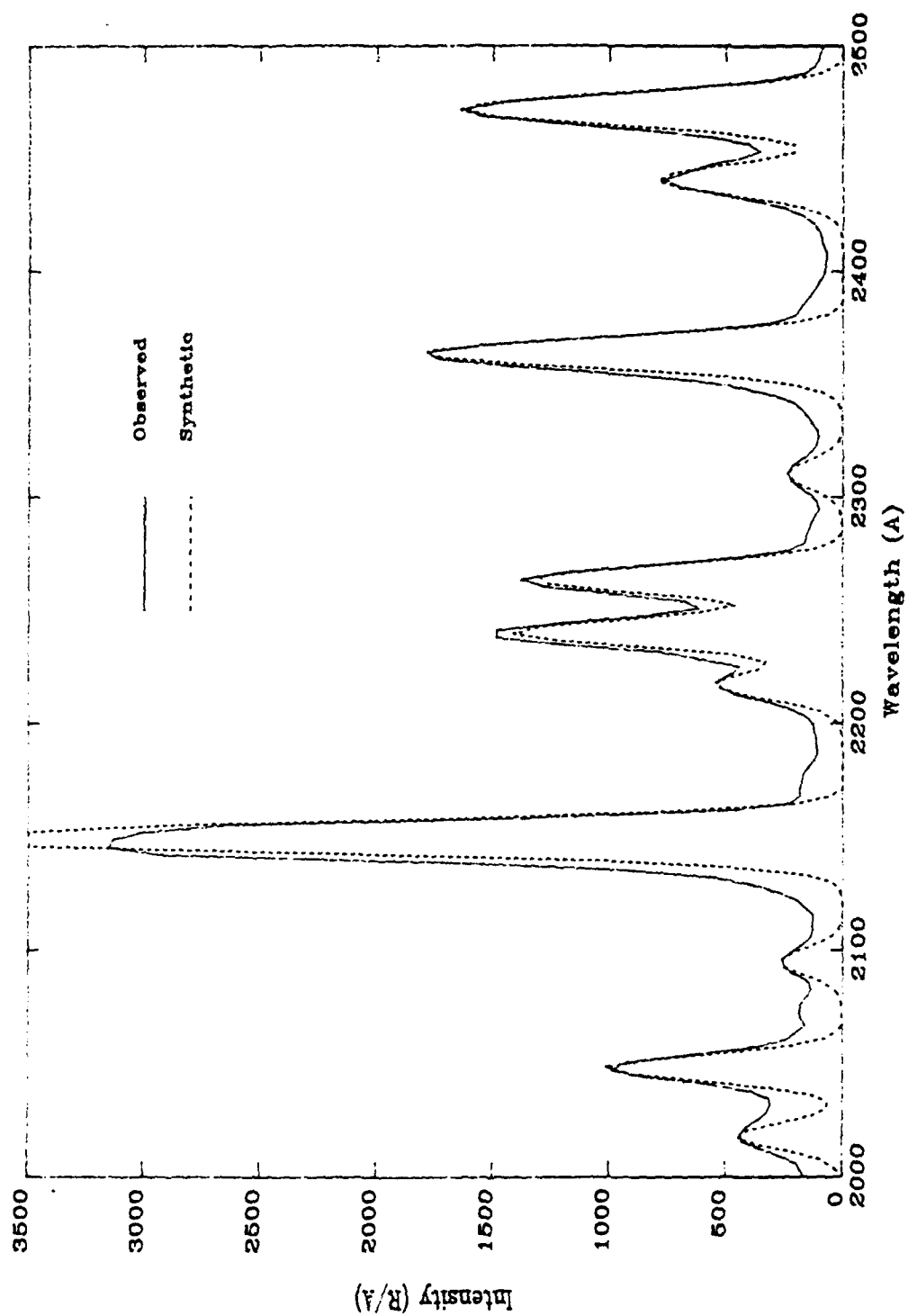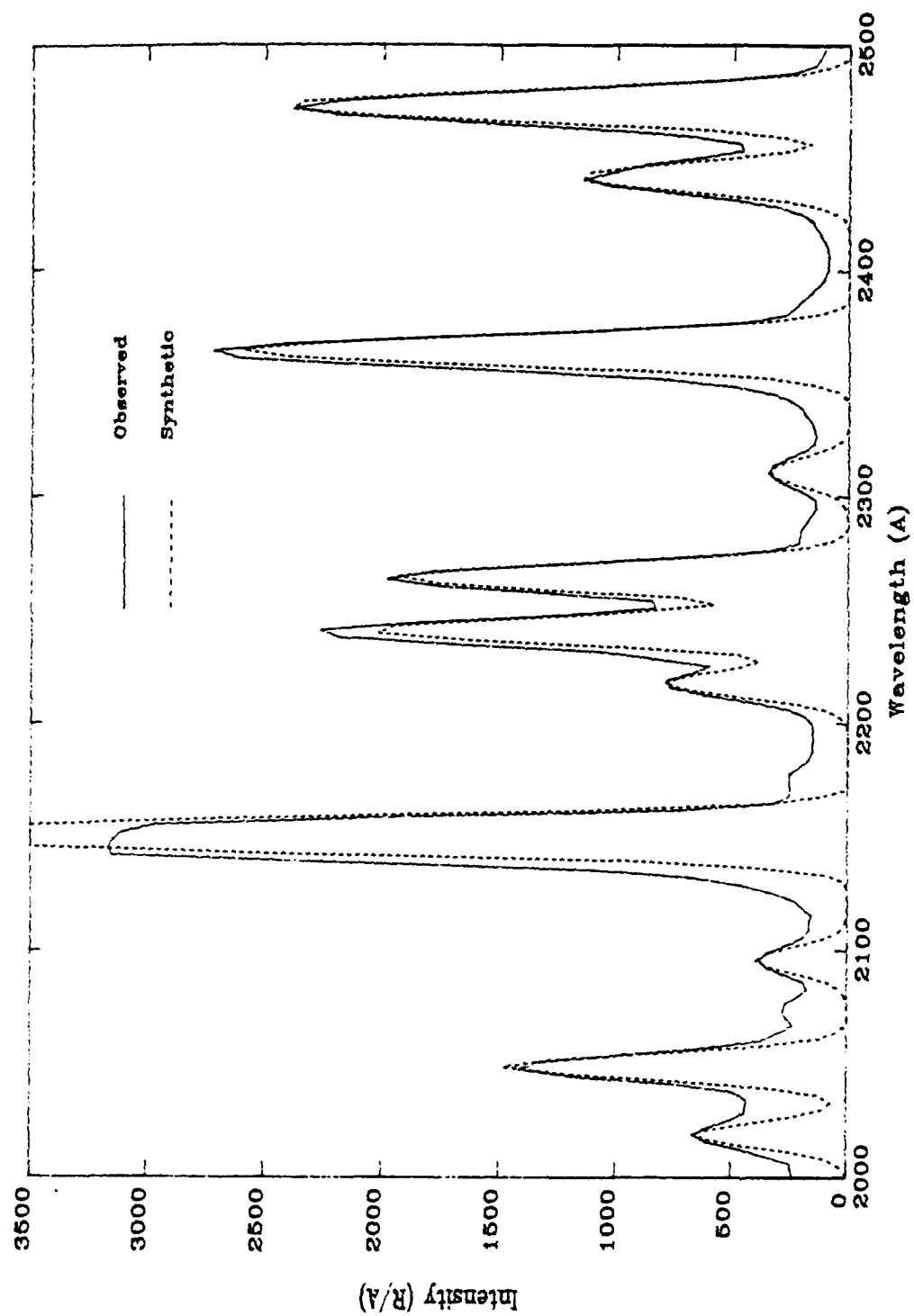
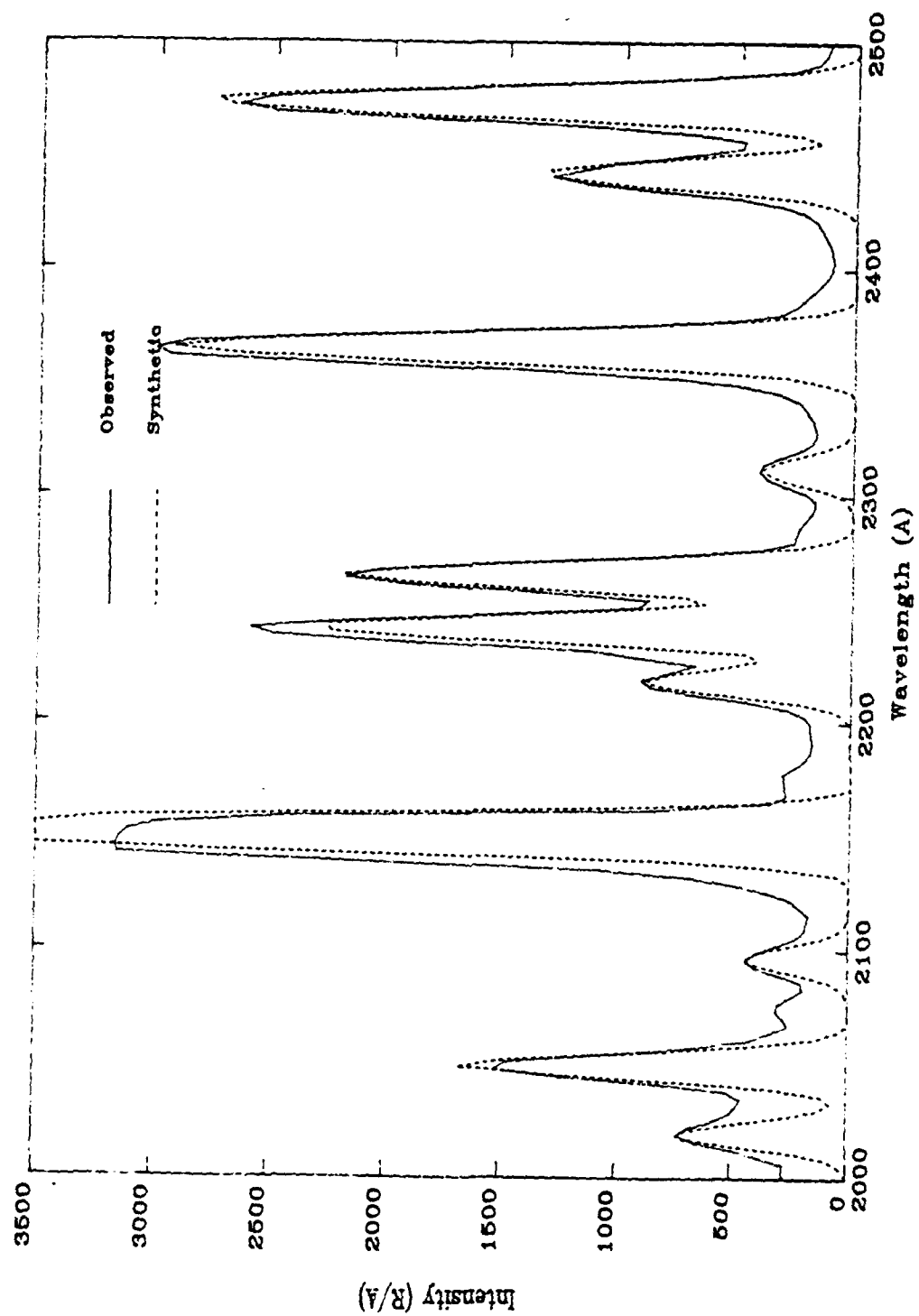**Figure 5-23** Comparison of Data and Synthetic Fit at 115 km (Down Leg)

53

Figure 5-24 Comparison of Data and Synthetic Fit at 105 km (Down Leg)

54

VI. CONCLUSION

A. SUMMARY OF FINDINGS

Ultraviolet emissions of the Earth's ionosphere in the wavelength range of 2000 Å to 2500 Å were analyzed. Eleven of the most prominent NO gamma and epsilon bands in the data were fit with synthetic spectra. An average column density was found for altitudes between 100 and 200 km which was larger than previous measurements. The atmospheric temperature profile was determined from the fit of the (1,0) gamma band. A comparison of the temperature profile to that predicted by the MSIS-83 model indicated a higher level of solar activity than the F10.7 would indicate. This conclusion was supported by the exceptionally high nitric oxide densities found.

The derived column densities were compared by v" progression. The data suggest that the Franck-Condon factors used in calculating the synthetic spectra underestimate emissions of the higher vibrational states of the gamma bands. Scale adjustments for the Franck-Condon factors were calculated and are shown in Figure 5- 10. These scale factors were applied to the synthetic spectra when determining the average column density.

B. RECOMMENDATIONS FOR FURTHER RESEARCH

The nitric oxide column densities found in this work produce an excellent fit to the data for the NO emissions. There are however, several areas of analysis which require further investigation. For example, the NO contributions can now be used in the analysis

of other emission features of the spectra. With the NO column densities as a starting point, N_2 synthetic spectra can be fit to the data to determine column densities for molecular nitrogen. This same technique can also be applied to the OII emission at 2470 Å. These steps are necessary to meet the overall goals of the experiment. The low altitude divergence between the observed γ (1,1) band and its synthetic fit should also be examined. As mentioned above, this difference may be indicative of an overlapping emission from some other source. The possibility of self absorption in the low altitude spectra of the γ (2,0) was mentioned. This effect could be investigated to determine if this is a significant factor in this data. Unfortunately, similar low altitude data for the γ (1,0) band is not available from this experiment. Additionally, completion of the post flight analysis should give some insight as to the apparent wavelength shift shown in Figure 5-1. Finally, future analyses of nitric oxide emissions should examine the observed and calculated Franck-Condon factors for the v″ progressions to establish the trend noted here.

BIBLIOGRAPHY

Bevington, P.R., *Data Reduction and Error Analysis for the Physical Sciences*, McGraw-Hill, Inc., 1969.

Bosserman, J.L., *Analysis of Thermospheric Dayglow Spectra From the Spacelab 1 Shuttle Mission*, Master's Thesis, Naval Postgraduate School, Monterey, California, December, 1989.

Bucsela, E.J., and Sharp, W.E., "The Relative Line Strength and Intensity of the NII 2143 Doublet," *Journal of Geophysical Research, 94*, 12069, 1989.

Cleary, D.D., *Analysis of Nitric Oxide Fluorescence Bands From High Latitude Rocke: Observations of the Thermospheric Dayglow*, Ph.D. Dissertation, University of Colorado, 1985.

Cleary, D.D., "Daytime High-Latitude Rocket Observations of the NO γ, δ, and ϵ Bands," *Journal of Geophysical Research, 91*, 11337, 1986.

Cleary, D.D., and Barth, C.A., "The NII 2143 Å Emission in the Dayglow," *Journal of Geophysical Research, 92*, 13635, 1987.

Eisberg, R., and Resnick, R., *Quantum Physics of Atoms, Molecules, Solids, Nuclei, and Particles*, Second Edition, John Wiley & Sons, Inc., 1985.

Gilmore, F.R., "Potential Energy Curves for N_2, NO, O_2, and Corresponding Ions," *Journal of Quantititive Spectroscopy and Radiative Transfer, 5*, 369, 1965.

Hedin, A.E., "A Revised Thermospheric Model Based on Mass Spectrometer and Incoherent Scatter Data; MSIS-83," *Journal of Geophysical Research, 88*, 10170, 1983.

Herzberg, G., *Molecular Spectra and Molecular Structure I. Spectra of Diatomic Molecules*, Second Edition, Van Nostrand Company, Inc., 1950.

McCoy, R.P., *Rocket Measurements of Thermospheric Odd Nitrogen and Comparisons With a Diffusive Transport Chemical Model*, Ph.D. Dissertation, University of Colorado, 1981.

NASA Technical Report 32822, *Ultraviolet Spectroscopy of Planets*, Barth, C.A., 1965.

Samson, J.A.R., *Techniques of Vacuum Ultraviolet Spectroscopy*, John Wiley & Sons, Inc., 1967.

Tascione, T.F., *Introduction to the Space Environment*, Orbit Book Company, Inc., 1988.

Tatum, J.B., "The Interpretation of Intensities in Diatomic Molecular Spectra," *The Astrophysical Journal Supplement Series*, *14*, 21, 1967.

Wallace, L., "Band-Head Wavelengths of C_2, CH, CN, CO, NH, NO, O_2, OH, and Their Ions," *The Astrophysical Journal Supplement Series*, *68*, 165, 1962.

INITIAL DISTRIBUTION LIST

1. Defense Technical Information Center   2
    Cameron Station
    Alexandria, Virginia 22304-6145

2. Library, Code 0142   2
    Naval Postgraduate School
    Monterey, California 93943-5000

3. Dr. K. Woehler, Chairman   1
    Physics Department, Code 61
    Naval Postgraduate School
    Monterey, California 93943-5000

4. Dr. David D. Cleary   5
    Physics Department, 61-CL
    Naval Postgraduate School
    Monterey, California 93943-5000

5. Dr. S. Gnanalingam   1
    Physics Department, 61-GM
    Naval Postgraduate School
    Monterey, California 93943-5000

6. Dr. R. McCoy   1
    Code 4140
    Naval Research Laboratory
    Washington D.C. 20375

7. Dr. K. Dymond   1
    Code 4141
    Naval Research Laboratory
    Washington D.C. 20735

8. LT Michael J. Clayton   1
    Physics Department
    United States Naval Academy
    Annapolis, Maryland 21402-5000